ARMY RESEARCH LABORATORY

Signal and Image Processing Algorithms for the U.S. Army Research Laboratory Ultra-wideband (UWB) Synchronous Impulse Reconstruction (SIRE) Radar

by Lam Nguyen

ARL-TR-4784 **April 2009**

NOTICES

Disclaimers

The findings in this report are not to be construed as an official Department of the Army position unless so designated by other authorized documents.

Citation of manufacturer's or trade names does not constitute an official endorsement or approval of the use thereof.

Destroy this report when it is no longer needed. Do not return it to the originator.

Army Research Laboratory
Adelphi, MD 20783-1197

ARL-TR-4784 **April 2009**

Signal and Image Processing Algorithms for the U.S. Army Research Laboratory Ultra-wideband (UWB) Synchronous Impulse Reconstruction (SIRE) Radar

Lam Nguyen
Sensors and Electron Devices Directorate, ARL

REPORT DOCUMENTATION PAGE	Form Approved OMB No. 0704-0188

1. REPORT DATE *(DD-MM-YYYY)*	2. REPORT TYPE	3. DATES COVERED (From - To)
April 2009	Final	

4. TITLE AND SUBTITLE	5a. CONTRACT NUMBER
Signal and Image Processing Algorithms for the U.S. Army Research Laboratory Ultra-wideband (UWB) Synchronous Impulse Reconstruction (SIRE) Radar	5b. GRANT NUMBER
	5c. PROGRAM ELEMENT NUMBER

6. AUTHOR(S)	5d. PROJECT NUMBER
Lam Nguyen	5e. TASK NUMBER
	5f. WORK UNIT NUMBER

7. PERFORMING ORGANIZATION NAME(S) AND ADDRESS(ES)	8. PERFORMING ORGANIZATION REPORT NUMBER
U.S. Army Research Laboratory ATTN: AMSRD-ARL-SE-RU 2800 Powder Mill Road Adelphi, MD 20783-1197	ARL-TR-4784

9. SPONSORING/MONITORING AGENCY NAME(S) AND ADDRESS(ES)	10. SPONSOR/MONITOR'S ACRONYM(S)
	11. SPONSOR/MONITOR'S REPORT NUMBER(S)

12. DISTRIBUTION/AVAILABILITY STATEMENT

Approved for public release; distribution unlimited.

13. SUPPLEMENTARY NOTES

14. ABSTRACT

The U.S. Army Research Laboratory (ARL), as part of a mission and customer-funded exploratory program, has developed a new low-frequency, impulse-based, ultra-wideband (UWB) synthetic aperture radar (SAR), which has been used as a test bed to support proof-of-concept demonstration for detecting concealed targets. The radar is intended to collect and process data at combat pace in an affordable, compact, and lightweight package. To achieve this, the radar is based on the synchronous impulse reconstruction (SIRE) technique, which uses several relatively slow and inexpensive analog-to-digital (A/D) converters to sample the wide bandwidth of radar signals. This report first briefly describes the key radar features directly related to the signal and image processing. The main section includes the signal processing steps to clean up noise and artifacts in radar data, and the image formation technique that SIRE employs. The report also details the Recursive Sidelobe Minimization (RSM) technique (patent pending), which was integrated with the standard SAR image formation algorithm to achieve a significant reduction in sidelobes and noise in the resulting SAR imagery. Finally, the report shows sample SAR images (in both forward-looking and side-looking modes) from recent experiments.

15. SUBJECT TERMS

Ultra-wideband radar (UWB), ground penetrating radar (GPR), SAR, image formation

16. SECURITY CLASSIFICATION OF:			17. LIMITATION OF ABSTRACT	18. NUMBER OF PAGES	19a. NAME OF RESPONSIBLE PERSON
a. REPORT	b. ABSTRACT	c. THIS PAGE			Lam Nguyen
Unclassified	Unclassified	Unclassified	UU	68	19b. TELEPHONE NUMBER (*Include area code*) (301) 394-0847

Standard Form 298 (Rev. 8/98)
Prescribed by ANSI Std. Z39.18

Contents

List of Figures

List of Tables

Acknowledgments

I would like to thank Mr. Marc Ressler, Mr. Francois Koenig, Mr. David Wong, Mr. Brian Stanton, Mr. Gregory Smith, Mr. Chi Tran, and Mr. Getachew Kirose of the U.S. Army Research Laboratory (ARL) for their professional and dedicated support with the radar measurement efforts.

INTENTIONALLY LEFT BLANK.

1. Introduction

The U.S. Army Research Laboratory (ARL), as part of a mission and customer funded exploratory program, has developed a new low-frequency, impulse-based, ultra-wideband (UWB) synthetic aperture radar (SAR). The radar has been used as a test bed to support proof-of-concept demonstrations for several programs (*1, 2*) for detecting concealed targets.

One of the primary features of the radar is the ability to collect and process data at combat pace in an affordable, compact, lightweight package. To achieve this, the radar is based on the synchronous impulse reconstruction (SIRE) technique, which uses several relatively slow and inexpensive analog-to-digital (A/D) converters to sample the wide bandwidth of radar signals.

This report first briefly describes the key radar features that are directly related to the signal and image processing issues. The main section includes the signal processing steps used to clean up noise and artifacts in radar data, and the image formation technique that SIRE employs. It also presents the Recursive Sidelobe Minimization (RSM) technique (patent pending), which was integrated with the standard SAR image formation algorithm to achieve a significant reduction in sidelobes and noise in the resulting SAR imagery. Finally, the report shows sample SAR images (in both forward-looking and side-looking modes) from recent experiments.

2. The SIRE Radar

In-depth details of the SIRE radar system have been discussed previously (*3*). In that paper, we summarized the system as follows. The radar is an impulse-based, UWB system. Downrange resolution is provided by the bandwidth of the transmitted monocycle pulse, which occupies the 300–3000 MHz frequency range. Since the radar was originally designed for the forward-looking mode, normal synthetic aperture approaches to imaging will not work, so instead we use a physical aperture using 16 identical receiving antennas. Each antenna feeds its own "receiver," in this case a base-band digitizing system based on low-cost commercial-off-the-shell (COTS) components. There are four receiving channels per data acquisition card (Quad board), and a timing and control card to provide the necessary clock references. Data for all four channels is integrated on each acquisition card and assembled waveforms are collected by a master controller. The six in-house designed boards are mounted in a modified Versa Module Europa (VME) chassis, which provides power and cooling as well as low-speed data bus connectivity. A custom-designed P2 backplane board supports critical timing signals. The data from the VME chassis, along with a global positioning system (GPS) time tag, are passed to a personal computer (PC), which acts as the operator control and status display (figure 1). Image processing

is done with a backprojection algorithm using data from a two-dimensional (2-D) synthetic aperture. All of these components are packaged onto a mobile test bed using a modified Ford Expedition. The complete integrated radar system is shown in figure 2.

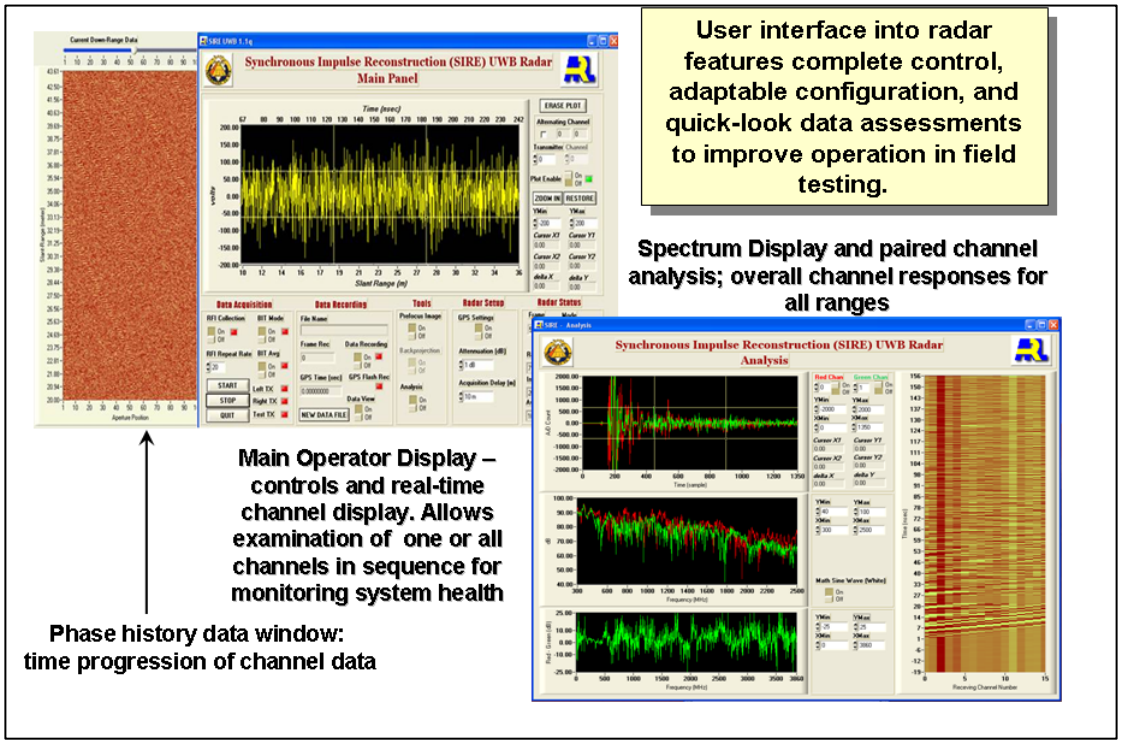

Figure 1. The ARL UWB SIRE radar operator control and status display.

Figure 2. The ARL UWB SIRE radar system integrated onto the Ford Expedition.

In this section, we briefly describe the key radar features, the configuration of the radar transmit and receive antennas, and the SIRE sampling technique, which are the features that are directly related to the signal and image processing issues. The detailed description of the radar hardware and software is described in reference 3 and are beyond the scope of this report.

Figure 3 shows the radar data imaging geometry in the forward-looking mode. The range coverage for this implementation is designed to have 26 m of range swath available, with a starting range of 8 m in front of the receiving antenna array and an ending range of 34 m. The radar is an impulse-based UWB system. The downrange resolution is a function of the signal bandwidth $(\Delta_r = \frac{c}{2B})$, where c is the speed of light and B is the bandwidth of the radar signal, which is the transmitted monocycle pulse that spans the 300–3000 MHz frequency range. For the forward-looking radar, we are more concerned with the cross-range resolution since we cannot generate a synthetic aperture in this direction. Within the 2-m aperture size constraint (the width of the vehicle), we can stack a number of receiving antennas. This array of physical receivers is used to form a cross-range aperture that is necessary to achieve the cross-range resolution of the forward-looking mode. For this implementation, we used the 16 Vivaldi notch antennas to form the receive array. The two transverse electromagnetic (TEM) horns are used for the transmit antennas.

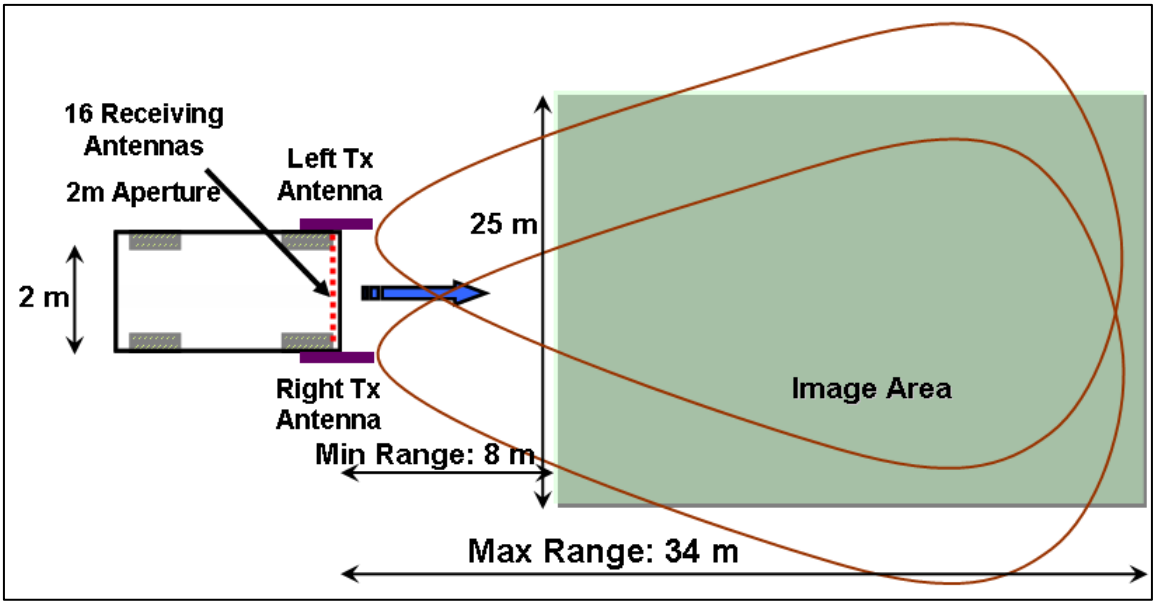

Figure 3. The ARL UWB SIRE radar imaging geometry in the forward-looking mode.

We have conducted a study to provide ourselves with insights into configuring our transmitter/receiver array and achieving a good cross-range resolution while minimizing the number of transmitting elements (*4*). In this work, we developed an analytical model that allows us to map the imaging geometry, which consists of the locations of transmitters, receivers, and the target in the spatial frequency domain. Figure 4a shows a configuration with an array of

receiving antennas and one transmitter placed at one end of the receiving array. Figure 4b shows the mapping of the Doppler information in the receiving signal of the imaging geometry configuration of figure 4a to the target spatial frequency samples. The angle span of these spatial frequency samples is proportional to the cross-range resolution of the resulting image since it represents the cross-range integration angle for the imaging process.

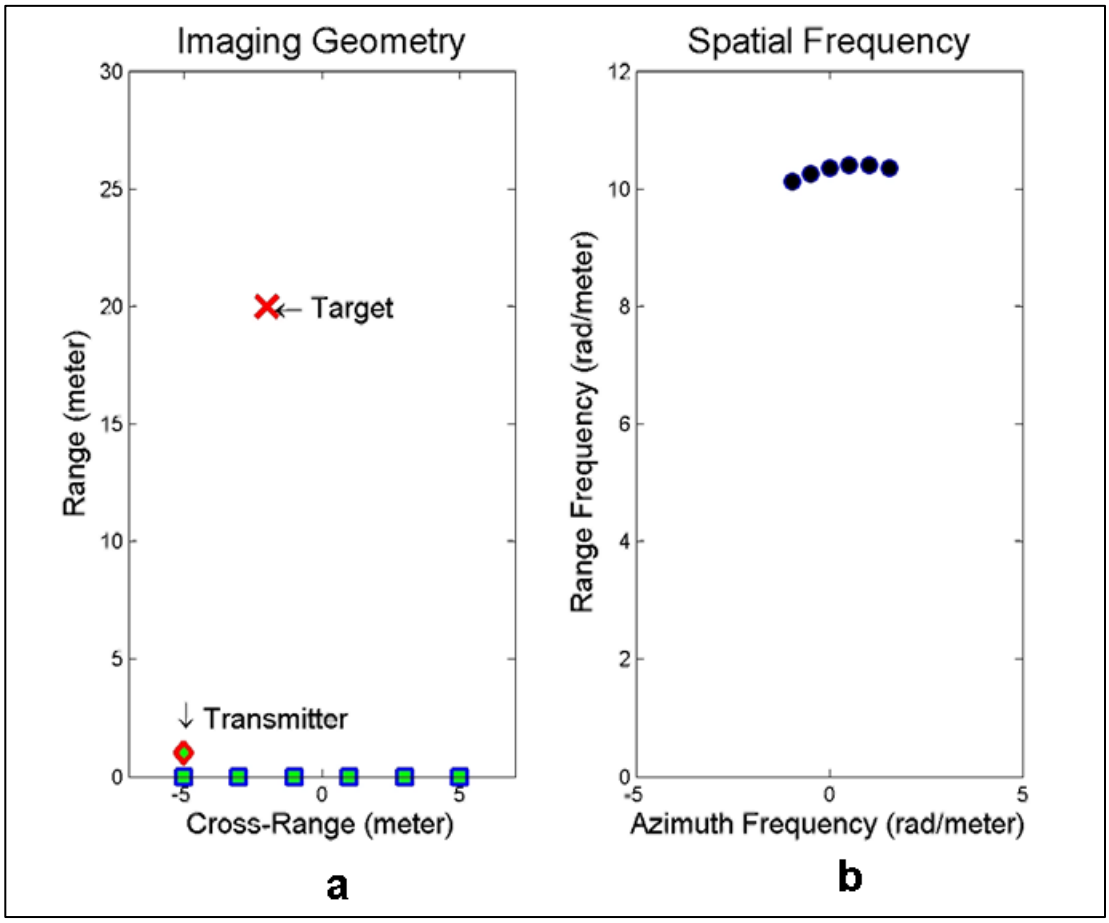

Figure 4. (a) Configuration with an array of receiving antenna and one transmitter placed at one end of the receiving array, and (b) the mapping of the Doppler information in the receiving signal to the target spatial frequency samples.

The next configuration is examined in figure 5. This configuration is similar to the one in figure 4, except that there is a transmit antenna located at each end of the receive array. The angle span of the target spatial frequency samples in this case is twice large as that of the case with only one transmitter.

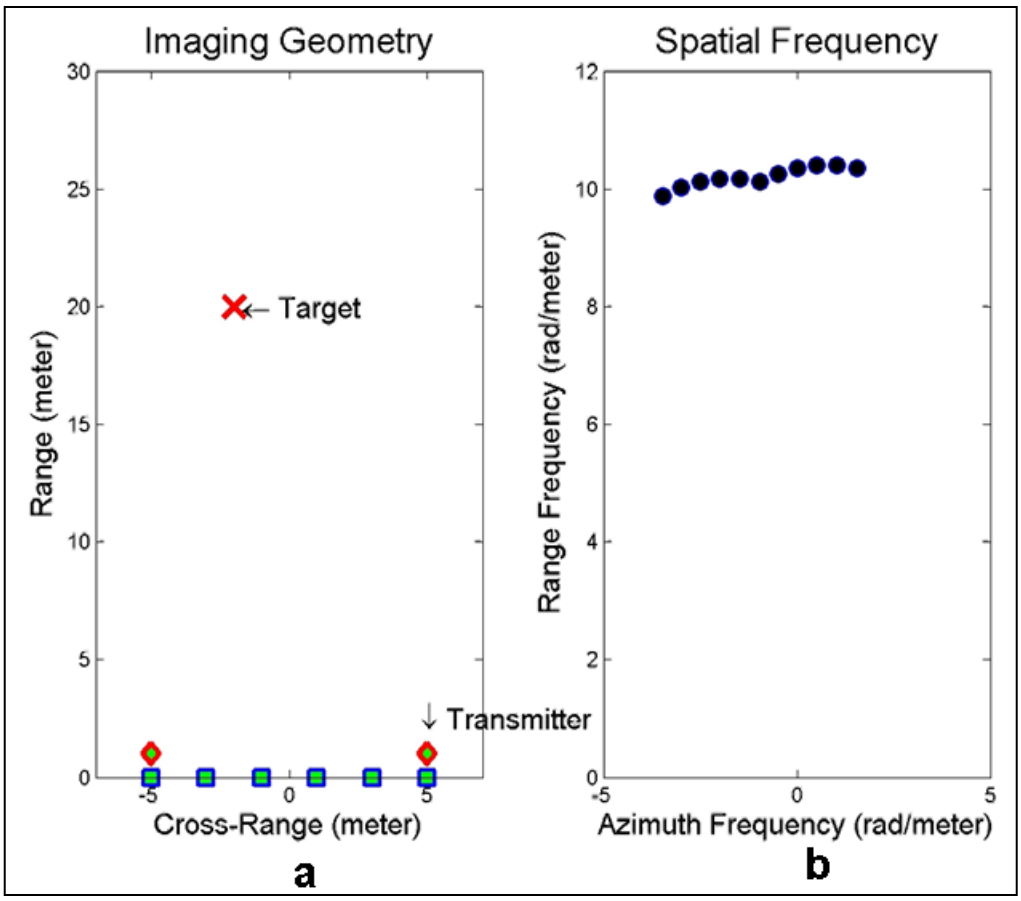

Figure 5. (a) Configuration with an array of receiving antenna with a transmitter placed at each end of the receiving array, and b) the mapping of the Doppler information in the receiving signal to the target spatial frequency samples.

Figure 6 shows another configuration with N transmitters and N receivers. The resulting angle span of the spatial frequency samples for this case is the same as the angle span for the configuration with two transmitters. Thus, the cross-range resolution is maximized by using only two transmit antennas, one located at each end of the receiving antenna array. To confirm this, we set up several simulation cases that correspond to the monostatic configuration and some variations of bistatic configurations. For each case, we generated a simulated range profile database and formed the corresponding image using the backprojection algorithm. We then compared the resolution of the point target from the images of various cases. Figure 7 shows the simulation results using four different configurations: (a) one transmitter located at the middle of the 16-antenna receiving array, (b) one transmitter at the end of the receiving array, (c) a monostatic configuration with 16 transmitters and 16 receivers, and (d) one with a transmitter at each end of the array. Again, the results show that with only two transmitters, located at each end of the receiving array (figure 7c), we can achieve the same cross-range resolution as the monostatic configuration with 16 transmitters (figure 7d). Figure 8 shows the expected cross-range resolution as a function of distance from radar to target for a fixed position measurement.

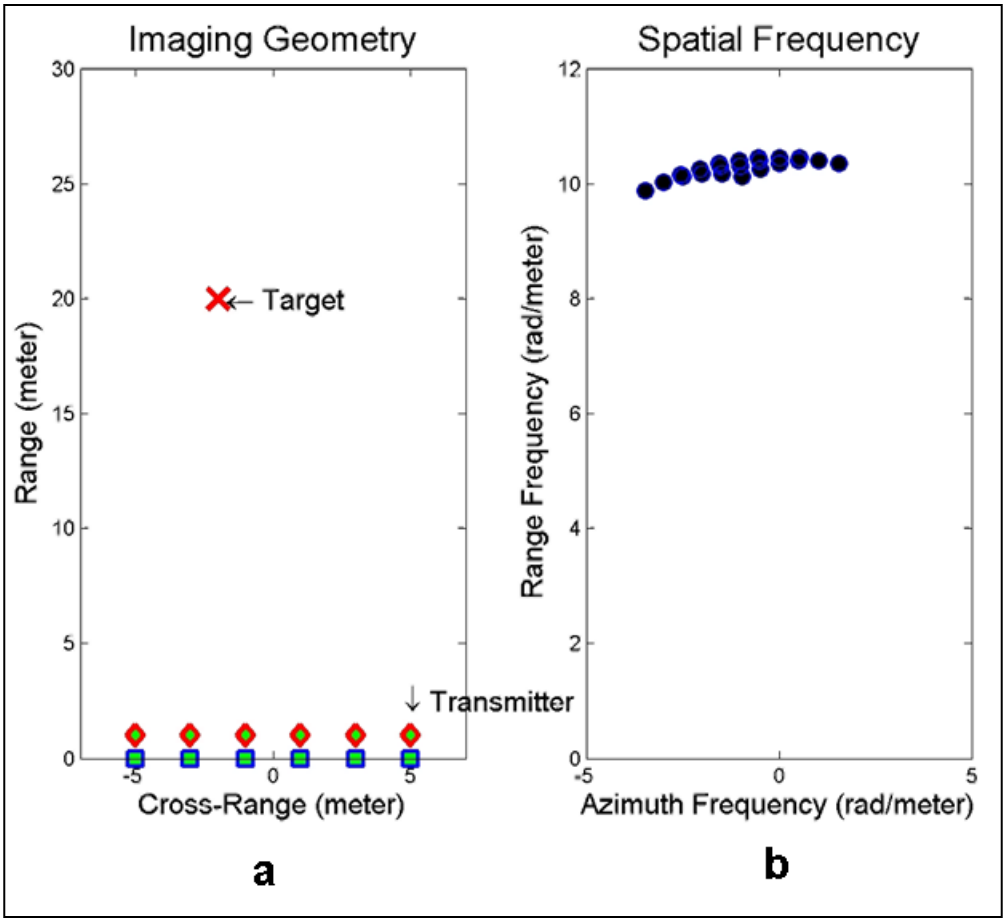

Figure 6. (a) Configuration with an array of N receiving antenna and N transmitters (monostatic), and (b) the mapping of the Doppler information in the receiving signal to the target spatial frequency samples.

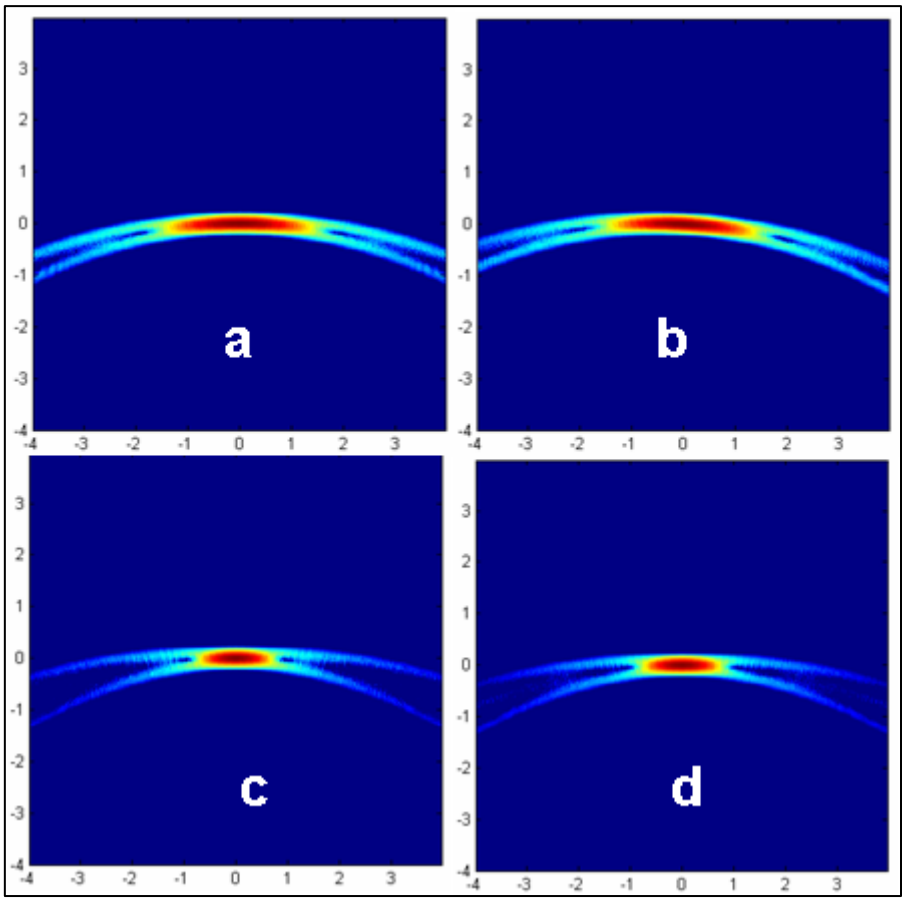

Figure 7. The simulation results using four different configurations: (a) one transmitter located at the middle of the 16-antenna receiving array, (b) one transmitter at the end of the receiving array, (c) a monostatic configuration with 16 transmitters and 16 receivers, and (d) a transmitter at each end of the array.

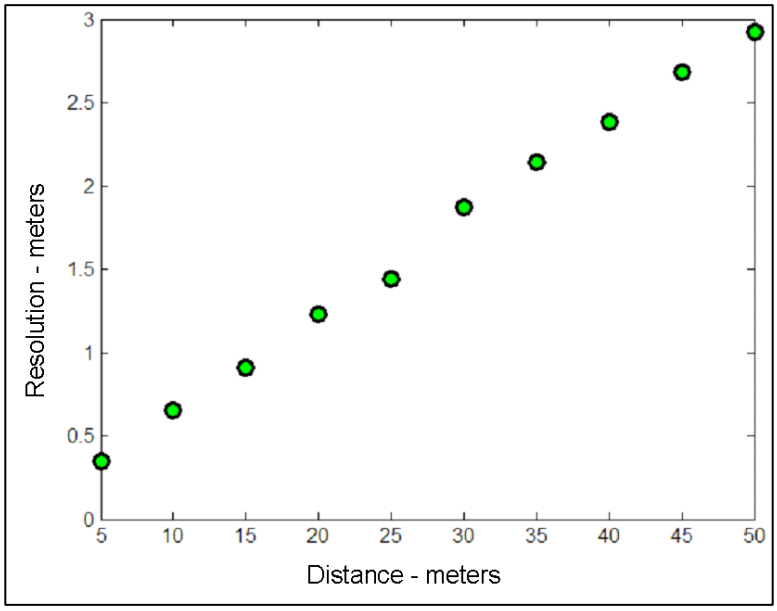

Figure 8. The expected cross-range resolution as a function of distance from radar to target for a fixed position measurement.

Each antenna feeds a base-band receiver/digitizer that integrates the data from a number of radar pulses before passing it on to the PC-based operator's console and display. The innovative ARL receiver design uses commercially available integrated circuits to provide a low-cost, lightweight digitizing scheme with an effective sampling rate of approximately 8 GHz. It employs an Analog Devices 12-bit 80 MHz analog-to-digital converter (ADC) to digitized returned radar signals; however, the ADC is clocked at the system clock rate of 40 MHz. From the basic sampling theory (*5*), it is not possible to reconstruct the wide-bandwidth signal (300 MHz–3000 MHz), since this ADC rate is much slower than the required minimum Nyquist sampling rate (6000 MHz). However, by using the synchronous time equivalence sampling technique, we can achieve a much higher equivalent sampling rate. Figure 9 provides a graphical representation of the SIRE data acquisition technique.

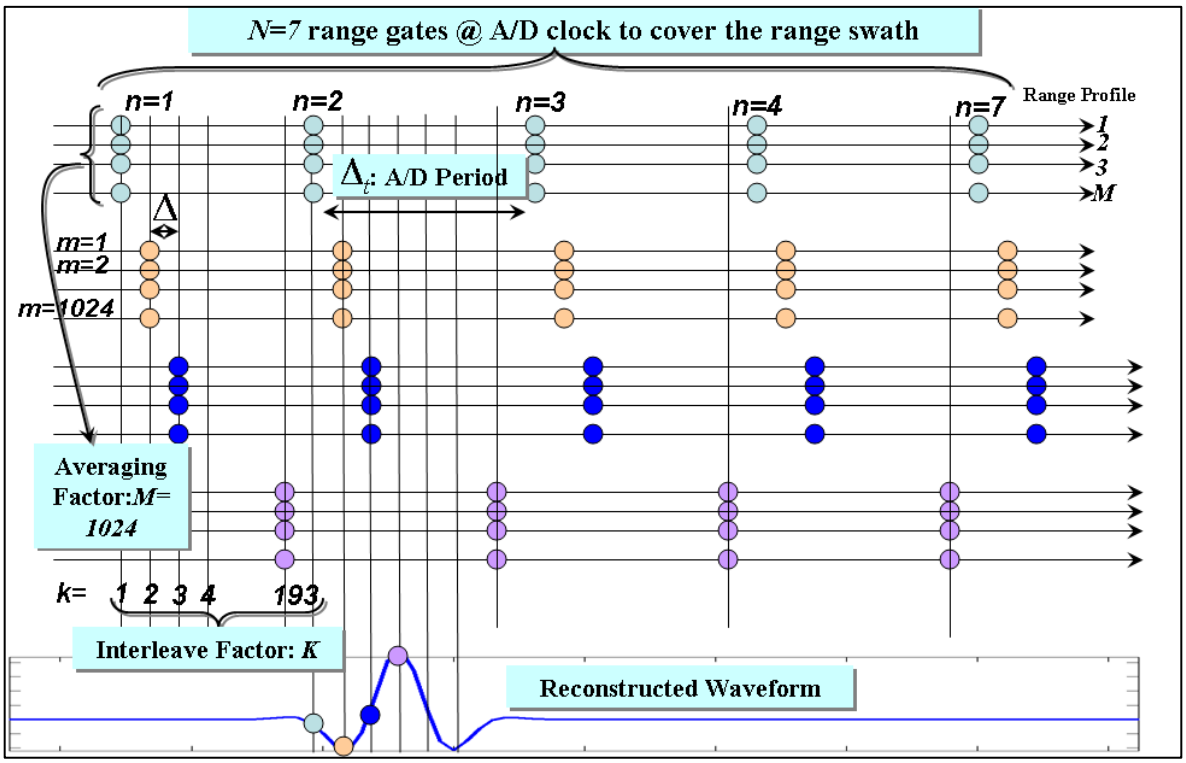

Figure 9. Graphical representation of the SIRE data acquisition technique.

The ADC sampling period is Δ_t; the value of this parameter in figure 9 is 25 ns, which corresponds to an A/D sampling rate of 40 MHz. The number of samples for each range profile is denoted by *N*, which is equal to 7 in our current configuration. This value corresponds to a range swath of 26 m. The system pulse repetition frequency (PRF) is 1 MHz. The system pulse repetition interval ($PRI = \frac{1}{PRF}$)—the inverse of PRF —is 1 ms. Each aliased (slowly sampled at A/D speed) radar record is measured *M* times (1024 in this example) and they are integrated to achieve higher signal-to-noise level. After summing M repeated measurements of the same range profile, the first range (fast-time) bin is increased by Δ. Thus, the next group of M range

profiles are digitized with a timing offset of Δ with respect to the transmit pulse. The parameter Δ represents a time sample spacing that satisfies the Nyquist criterion for the transmitted radar signal. This time sample spacing is 129.53 ps, which corresponds to a sampling rate of 7.72 GHz. This effective sampling rate is sufficient for the wide-bandwidth radar signal (300 MHz–3000 MHz). The number of interleaved samples is

$$K = \frac{\Delta_t}{\Delta}, \tag{1}$$

which is 193 in figure 9. After *K* groups of *M* pulses are transmitted and the return signals are digitized and summed by the Xilinx Spartan 3 field-programmable gate array (FPGA), this results in a radar record of $N \cdot K$ samples with an equivalent of fast sample spacing of Δ. The total time to complete one data acquisition cycle is $N \cdot K \cdot PRI$, which is 197.6 ms in this case. It should be noted that during the entire data acquisition cycle period (197.6 ms), the relative position between the radar and the targets is assumed to be stationary. Table 1 summarizes the parameters used by the SIRE data acquisition technique.

Table 1. Summary of data acquisition parameters.

Radar *PRF*	1 MHz
Radar *PRI*	1e-6 s
ADC sampling rate	40 MHz
ADC sampling period	25 ns
Number of ADC (slow) range gates (*N*)	7
Interleaving factor (*K*)	193
Number of repeated measurements for averaging (*M*)	1024
Total number of range gates ($N \cdot K$)	1351
Effective sampling period (time-equivalent)	129.53e-12 s
Effective sampling rate (time-equivalent)	7.72 GHz
Total data acquisition time	197.6 ms

Figure 10 shows the SIRE transmitting pulse in the time-domain and frequency-domain. From this figure, the 6-dB bandwidth of the transmitting pulse is from 300 MHz to almost 1900 MHz. The transmitting spectrum is further modified by the transmitting TEM horn antenna, which reduces the gain of the lower frequency band under 1.5 GHz. Figure 11 shows a false color plot of one complete frame of radar data: 16 receiving records using the left transmitter and 16 receiving records using the right transmitter. This raw radar data frame is displayed before any signal processing step. It shows the DC offsets in several receiving channels. Figure 12 shows the same data visualization of many radar data frames when the radar continuously transmits and receives data while the platform moves toward the imaging area. The visualization shows traces of the returns from several targets with a large radar cross section (RCS).

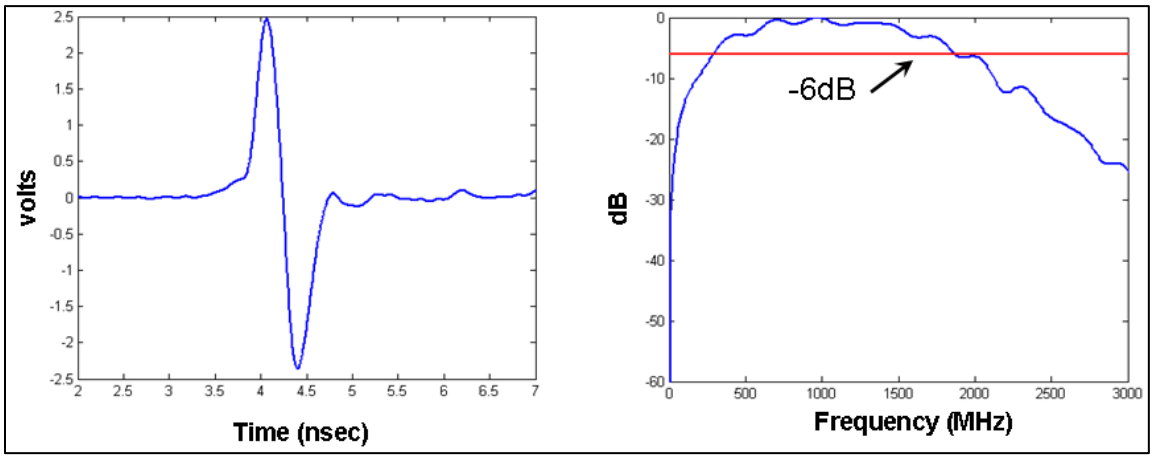

Figure 10. The SIRE transmitting pulse in the time-domain and frequency-domain.

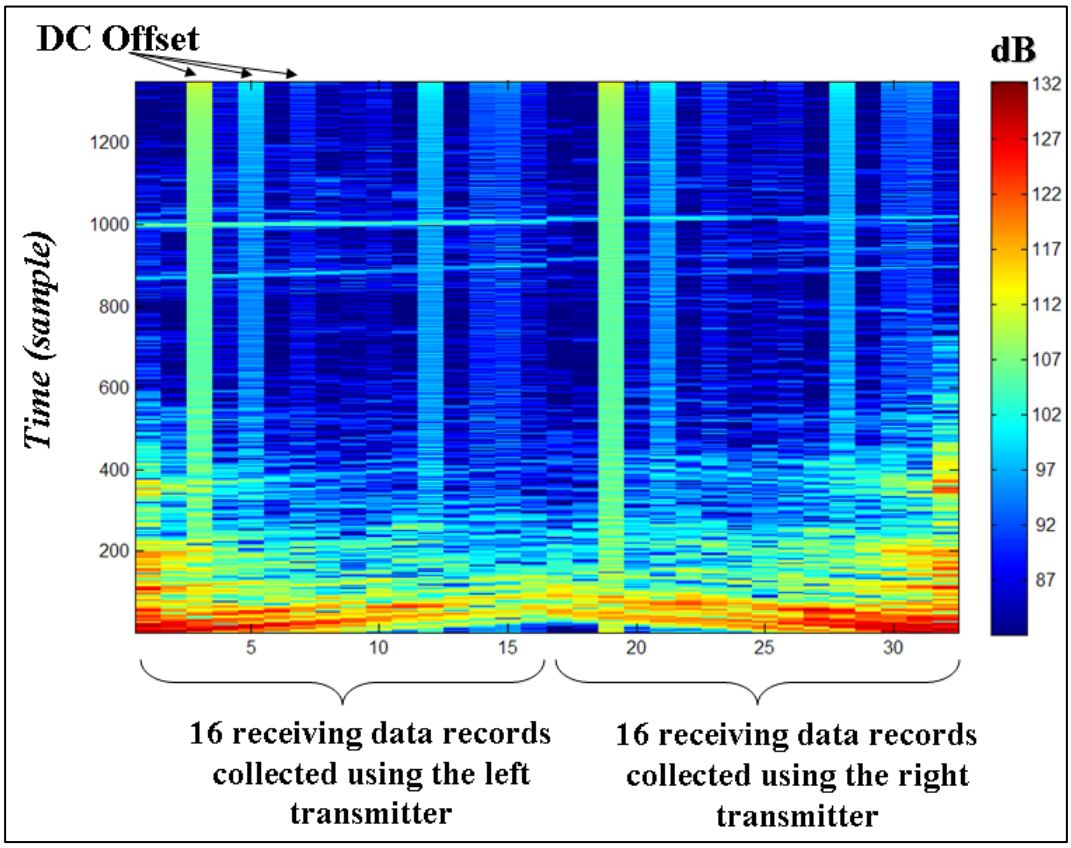

Figure 11. False color plot of one complete frame of radar data: 16 receiving records using the left transmitter and 16 receiving records using the right transmitter.

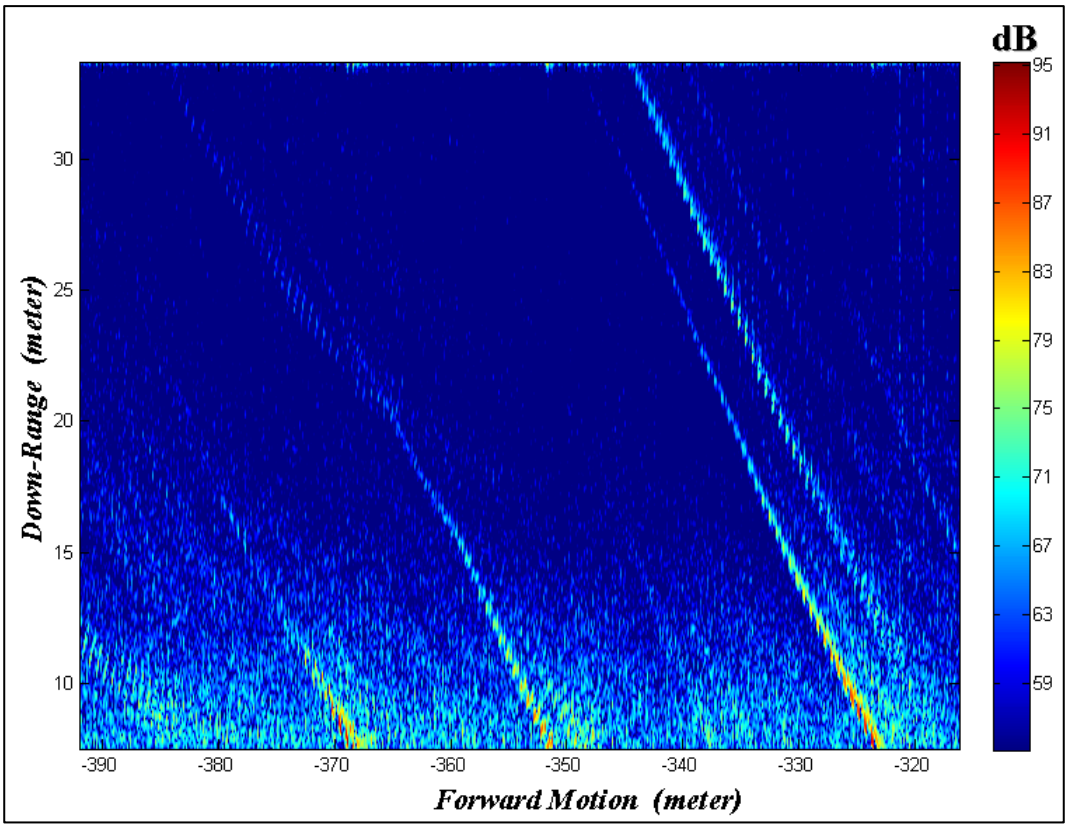

Figure 12. Data visualization of many radar data frames when the radar continuously transmits and receives data while the platform moves toward the imaging area.

3. Signal and Image Processing

ARL has developed a suite of processing algorithms to process SIRE radar data and form SAR imagery in both forward-looking and side-looking modes. There are three main sections: radar position data processing, signal processing, and image formation. Figure 13 is a block diagram that shows the overall processing steps for the SIRE radar data in the forward-looking mode.

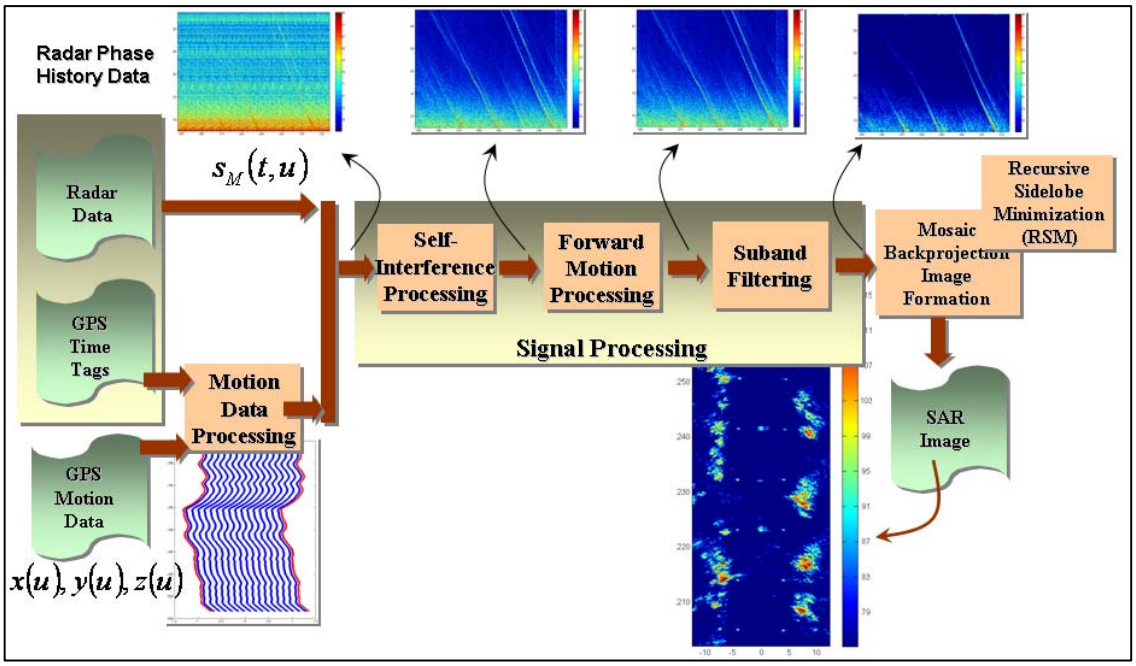

Figure 13. Block diagram of the overall processing steps for the SIRE radar data in the forward-looking mode.

3.1 Radar Position Data Processing

The radar employs two Ashtech Z-surveyor GPS units in the differential mode to track the radar location that is necessary for the image formation algorithm. The GPS measurement system consists of two subsystems: a rover station, whose antenna is located with the radar's antenna frame, and a base station at a fixed location in the field. GPS data are recorded by both the rover receiver and the base station receiver. Both units operate independently and continuously track as many as 12 channels of satellites in orbit. The SIRE radar system supports the data collection in two modes: post-processing and real-time.

In the post-processing mode (figure 14), measurements from the rover receiver are recorded independently and the GPS data stream from each receiver is recorded in its own flash memory. To synchronize the GPS measurement with the radar operation, the SIRE data acquisition and control system sends a trigger pulse to the rover receiver at the midpoint of each data acquisition cycle. In response to the trigger signal, the rover receiver reports back to the data acquisition system with the GPS time tag via the RS232 interface. The data acquisition then embeds this GPS time tag information into the radar data stream for synchronization purpose. After the radar measurement operation is completed, data from the GPS rover and base station receivers are differentially processed using the Wavepoint's GrafNav software to generate the position data within an accuracy of a few centimeters. With the differentially processed GPS data available, we can then compute the radar (x, y, z) coordinates that are synchronized with the radar data measurements by using the GPS time tags embedded in the radar data stream and performing the table lookup and interpolation of the GPS data.

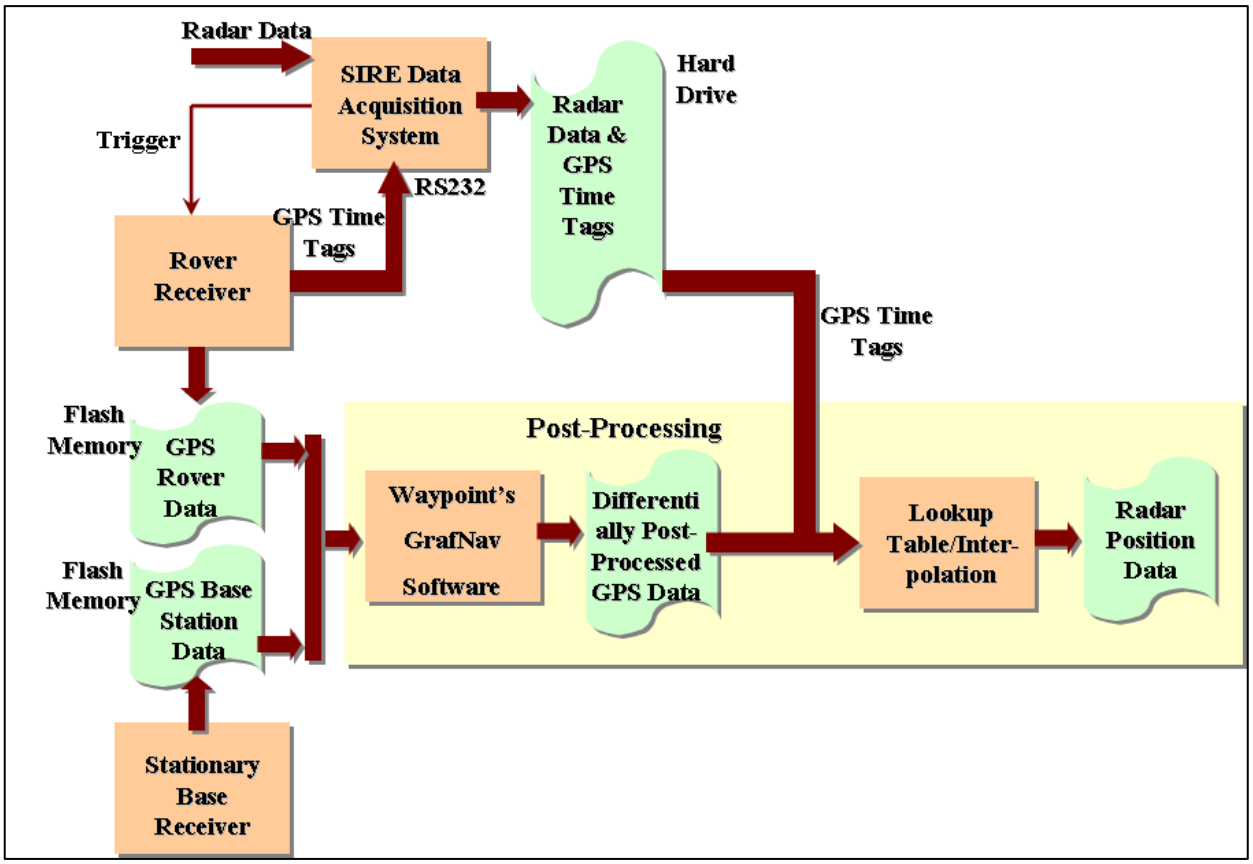

Figure 14. Processing of radar position data in the post-processing mode.

In real-time mode (figure 15), both the rover and the base station receivers record the GPS data independently as in the post-processing mode; however, data from the base station are sent to the rover via a radio frequency (RF) link. The rover receiver then combines its measured data with the base station receiver data, and differentially processes them to generate accurate GPS position information in real time. The two data stream—GPS time tags and the differentially processed GPS data—are sent to the data acquisition and control system by the rover receiver via two RS-232 interfaces. As in the post-processing mode, the radar signal and image processor computes the radar (x, y, z) coordinates that are synchronized with the radar data measurements by using the GPS time tags and performing the table lookup and interpolation processes. The difference is that the table lookup and interpolation of the GPS data are performed in real time in this case.

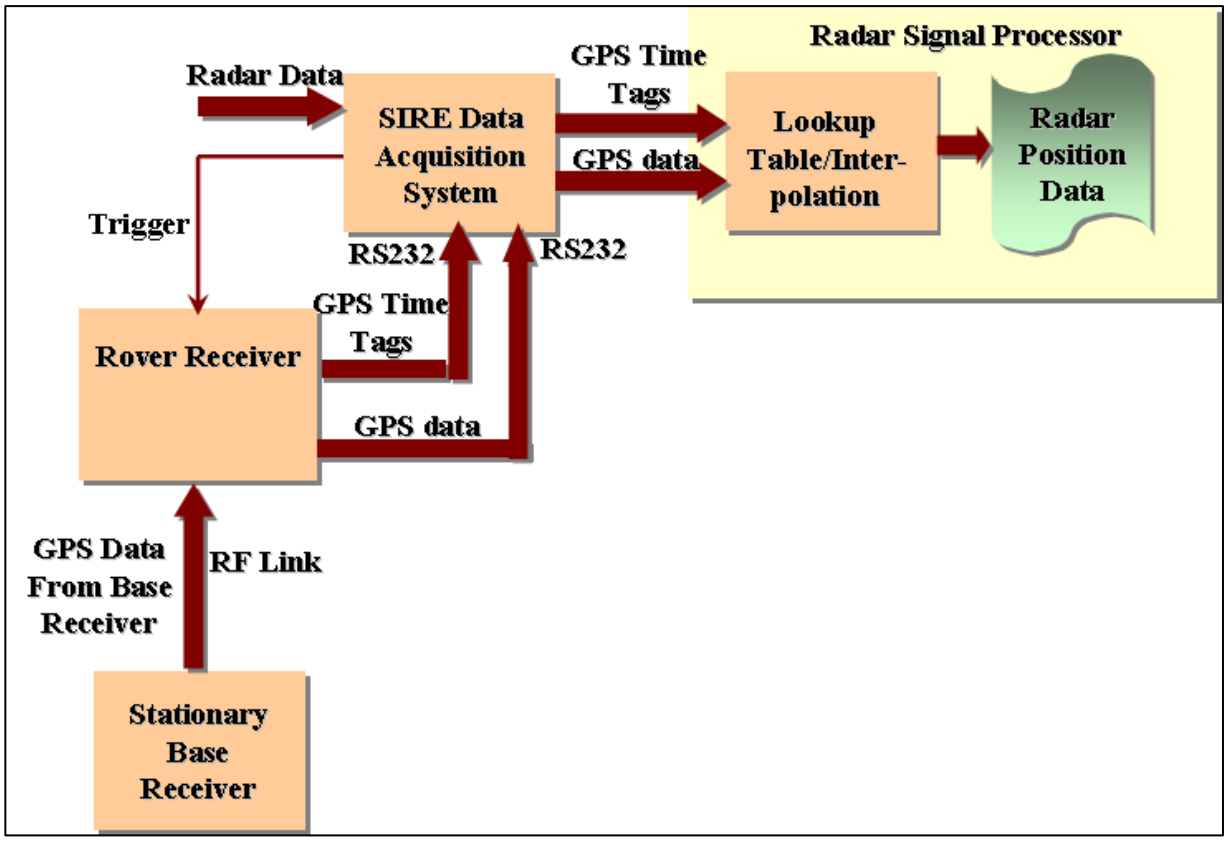

Figure 15. Processing of radar position data in real-time processing mode.

Once the radar position information is available, the coordinates of the two transmitters and the 16 receivers must be derived as required by the imaging process. Note that the GPS coordinates that were measured and computed (figures 14 and 15) only represent the positions of one point on the vehicle, which is the GPS rover antenna. The rover antenna is located at approximately the center of radar receiver antenna array. Since the locations of the two transmitter antennas and the receiver antennas have fixed offsets (in three dimensions) with respect to the rover antenna, in theory, it is possible to derive the coordinates of all transmit and receive antennas from the coordinates of the rover antenna. However, in practice, the motion of the vehicle usually does not follow a straight path. Three components of the velocity vector are required to estimate the coordinates of all individual antennas. Among these three components, the heading information from the velocity vector is most important since a small variation in the heading results in a large error. For example, a change of 5° in the heading corresponds to a shift of 1.75 m for the imaging pixels 20 m in front of the vehicle. The phase coherency between data frames will be degraded and the quality of the resulting SAR image will suffer. However, using the radar position data, we can estimate the heading information of the platform, and then use this information to estimate the coordinates for 2 transmit antennas and 16 receive antennas. A simple smoothing filter or a more sophisticated Kalman filter can be used to filter the position data and estimate the heading information. In our current implementation, we have demonstrated good results using a

simple smoothing filter. Figure 16 shows the (x, y)coordinates of 2 transmit antennas (red color) and 16 receive antennas (blue color) as the radar platform moves along a road. Figure 17 shows a side-by-side SAR image comparison: the left SAR image does not include the heading information, the right SAR image is focused using the estimated heading information. Some targets are highlighted with the rectangular bounding boxes. The targets in the right SAR image are much more focused and have higher amplitudes.

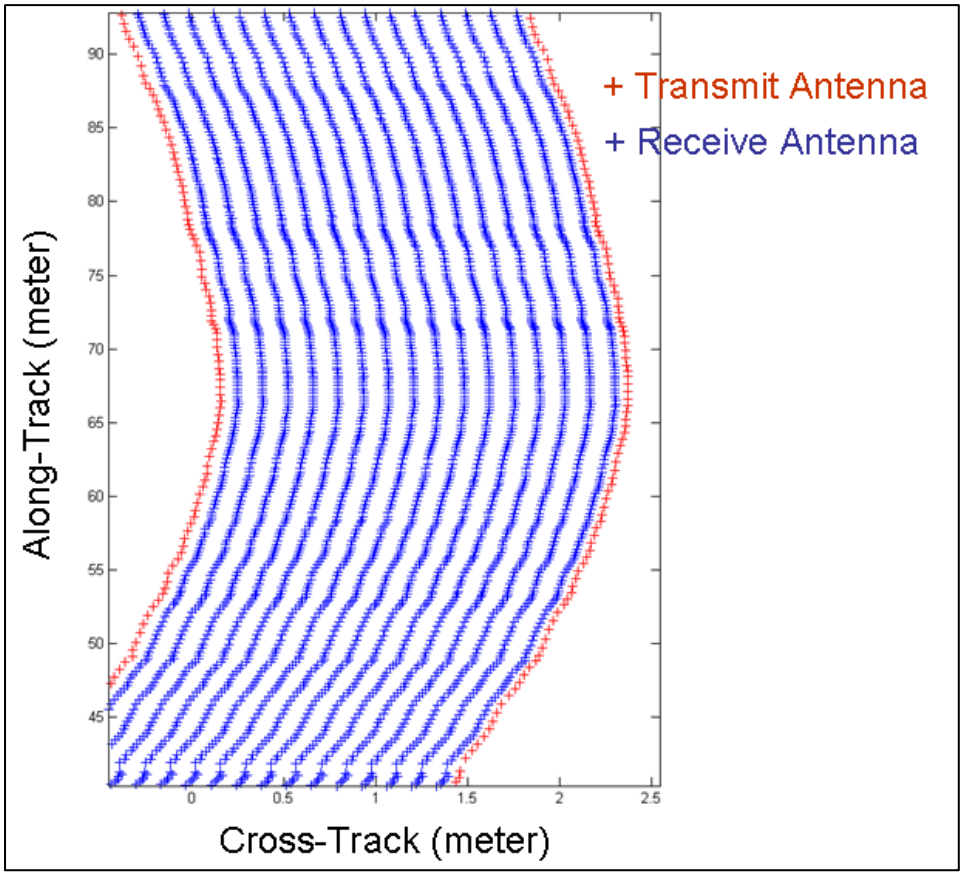

Figure 16. Coordinates of 2 transmit antennas (red color) and 16 receive antennas (blue color) as the radar platform moves along a road.

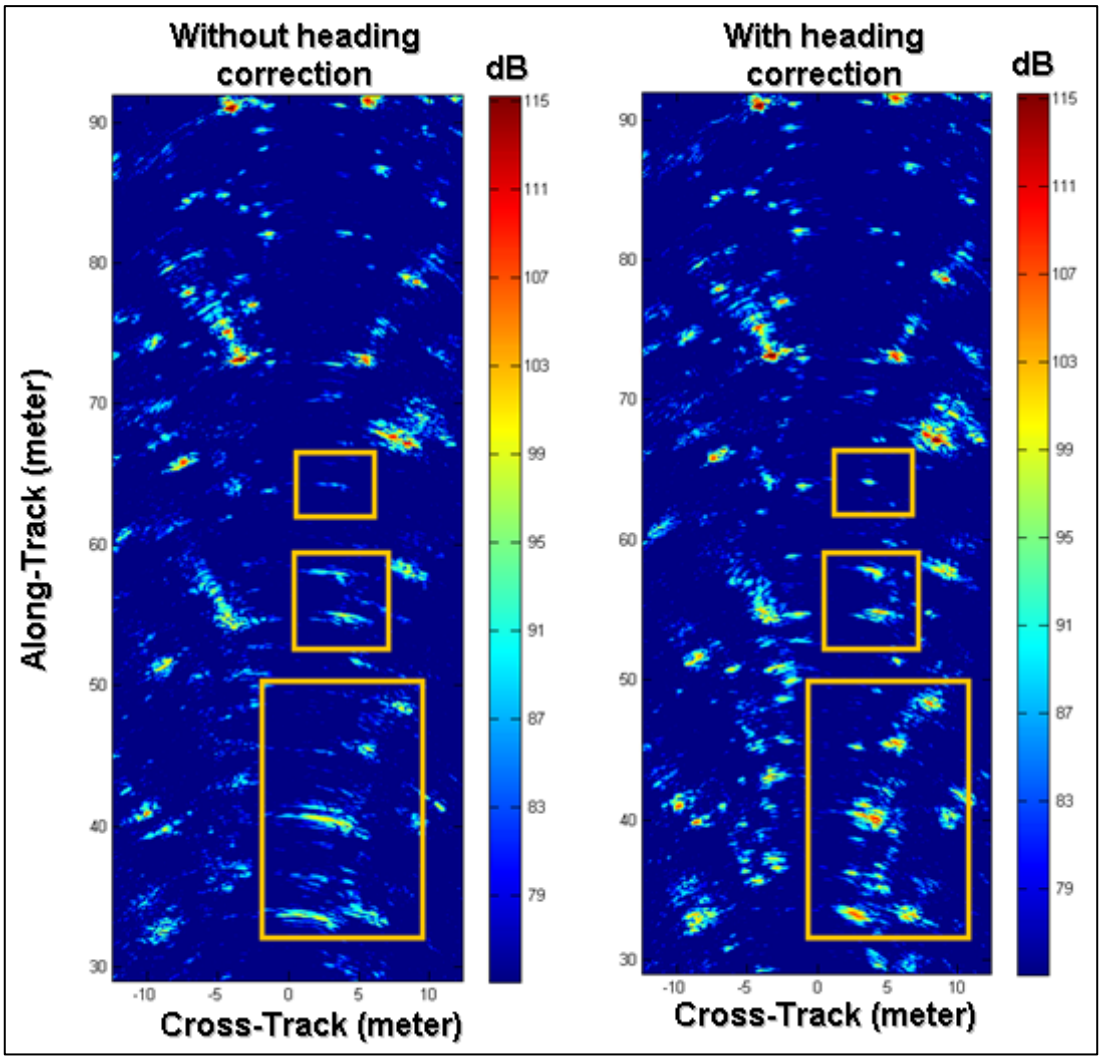

Figure 17. SAR image comparison: the left SAR image does not include the heading information and the right SAR image is focused using the estimated heading information.

3.2 Suppression of RFI Signal

An important factor that has adverse effect in the quality of UWB SAR imagery is the presence of powerful RF interference (RFI) sources such as radio and TV signals, wireless communication services, etc., in the RF band. We have developed RFI suppression techniques in the past (*6, 7*) to suppress/extract these interference signals from the UWB radar data. These techniques rely on the ability to reconstruct the RFI frequency contents from the acquired data. However, using the sampling technique that the SIRE radar employs that allows us to sample wide bandwidth signals with relatively slow and inexpensive A/D, the RFI signals cannot be reconstructed from the acquired data. Instead, their frequency contents spread throughout the radar transmission band. Previous RFI techniques would not work for this situation. Fortunately, the suppression of the RFI signals is performed by the SIRE data acquisition scheme described in section 2 (figure 9).

We have conducted a study and reported the characteristics of the reconstructed RFI signals using this data acquisition scheme (*8*). Some results are highlighted here. Figure 18 shows the frequency domain of the simulation results that consist of eight sources representing both narrowband and wideband RFI signals. The black curve shows the original unaliased frequency contents of the RFI signal, which are obvious in the spectrum. The blue curve shows the frequency contents of the reconstructed RFI signal using the SIRE data acquisition scheme with $M = 1$ (the parameter M is the averaging factor that is described in section 2, table 1 and figure 9). The red curve shows the frequency contents of the reconstructed RFI signal using the SIRE data acquisition scheme with $M = 1000$, with the suppression of 30 dB of the RFI energy level. Figure 19 shows the reduction of the RFI energy as a function of the averaging factor M .

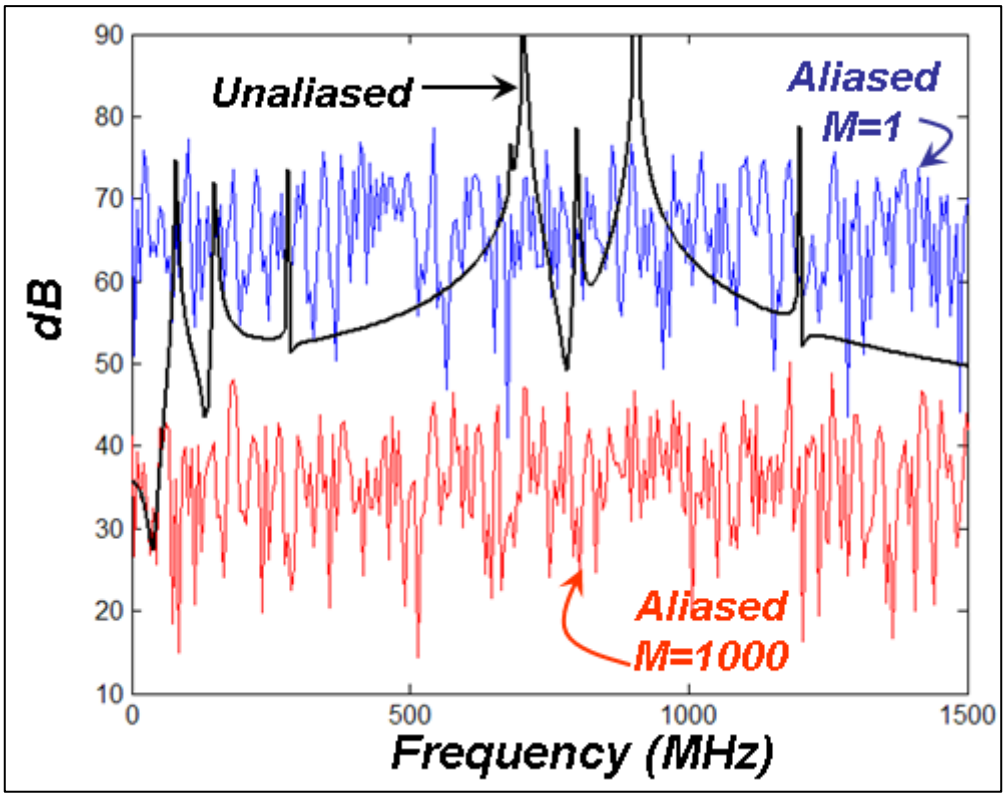

Figure 18. Frequency domain of the simulation results that consist of eight sources representing both narrowband and wideband RFI signals.

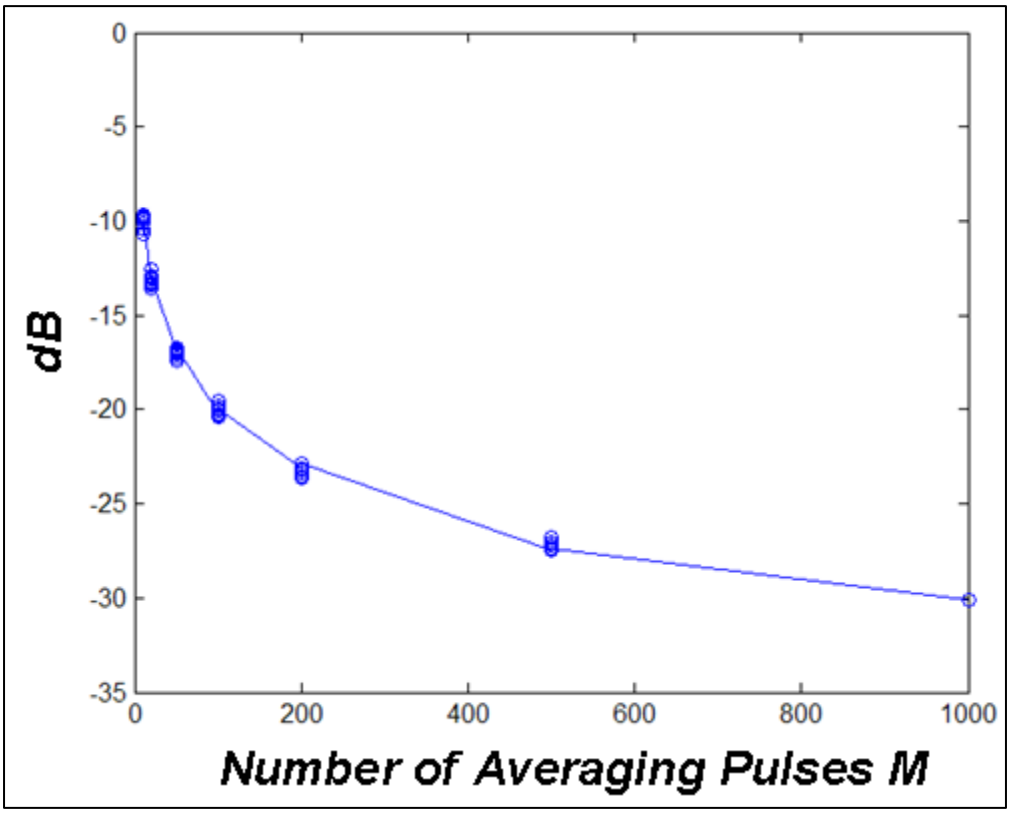

Figure 19. The reduction of the RFI energy as a function of the averaging factor.

3.3 Suppression of Self-interference Signal

Figure 20 shows a false color plot of a group of 4500 downrange radar records vs. aperture position. It is obvious from the figure that low-frequency ripples of the self-interference signals appear as the horizontal stripes and dominate the data visualization. For each radar range profile, the self-interference signal begins at early range gates and propagates throughout the entire record. They are very large in amplitude and thus even targets with high RCS are obscured under the presence of self-interference signals. One of the sources of the self-interference signal is that the pulses emitted from the transmitter excite the radar supporting structure and surrounding objects. This causes a “ring-down” to be superimposed on the data. In addition, any mismatch between system components could cause this low frequency ring-down to occur.

ARL has been employing the following technique to remove these unwanted signal components from radar data (*9*). The main idea behind the self-interference removal technique is that the interference signal is quasi stationary, while the targets’ backscatter signals are not. Thus, averaging all the downrange records over a long period of time will give us a good estimate of the self-interference signal. In reality, the interference signal changes its characteristics (phase, amplitude, frequency contents) with time, especially with the motion of the radar. Therefore, a

sliding window approach is chosen to adaptively estimate the interference signal's template. The algorithm forms a running average of radar data across the aperture, estimates the amplitudes and phases of unwanted components, and coherently removes these components from radar data.

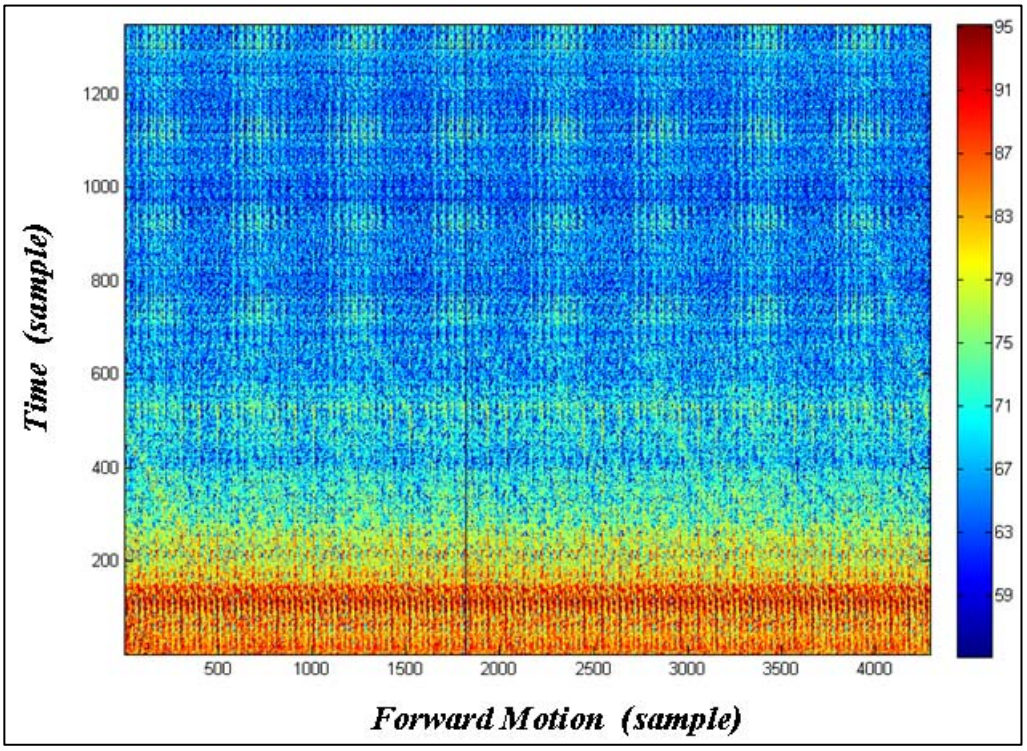

Figure 20. Data visualization for group of 4500 down range radar records versus aperture position.

Let Si be a downrange record at ith position in the aperture. The interference template at this ith aperture position is

$$T_i[j] = \frac{1}{w} \sum_{k=i-w/2}^{i+w/2} S_k[j] \qquad j=1, \text{n} \tag{2}$$

where n is the number of samples in a downrange record, and w is the window length.

The quadrature component of the interference template is computed as the Hilbert transform of Ti

$$TH_i = Hilbert(T_i) \tag{3}$$

A multi-dimensional signal space containing all the unwanted components is now formed. This serves as a basis to compute all the unwanted components contained in any radar downrange record. The first component of the signal space represents the DC component. This component will help to remove any DC bias included in the radar signal. The second vector represents a ramp to help remove the change in DC bias. The third and fourth components are the interference template and its Hilbert transform. The projection of the radar downrange record on

these two components will give a good estimate of phase and amplitude of the interference signal embedded in the radar record. The following matrix represents a signal space for the unwanted signal at position i in the aperture.

$$\underline{\mathbf{B_i}} = [\ \underline{\mathbf{DC}}\ \ \underline{\mathbf{R}}\ \ \underline{\mathbf{T_i}}\ \ \underline{\mathbf{TH_i}}\ ] \tag{4}$$

where $\underline{\mathbf{B_i}}$ is the basis for the interference signal space at aperture position i, DC is a constant vector of i, R is a ramp vector, and $\underline{\mathbf{T_i}}$ and $\underline{\mathbf{TH_i}}$ are the interference template and its Hilbert transform, respectively.

The next step is to transform the previously mentioned interference signal space basis into an orthonormal basis. This will allow us to extract exactly the amount of each interference component from the signal. The Gram-Schmidt procedure is used to transform the previously mentioned basis matrix into an orthonormal basis.

Let $\mathbf{X_k}$ (k=1,m) be the basis matrix into an m-dimensional vector space. The orthonormal basis is derived as follows:

$$\begin{aligned}
&Y1 = X1 \\
&Y_2 = X_2 - \frac{Y_1.X_2}{Y_1.Y_1}.Y_1 \\
&\ldots\ldots\ldots\ldots\ldots \\
&Y_m = X_m - \frac{Y_{m+1}.X_m}{Y_{m-1}.Y_{m-1}}.Y_{m-1} - \frac{Y_1.X_m}{Y_1.Y_1}.Y_1 \\
&G_k = \frac{Y_k}{\|Y_k\|}
\end{aligned} \tag{5}$$

where $\underline{\mathbf{G_{k\ (k=1,2\ldots..,m)}}}$ is the orthonormal basis of the vector space.

Using this procedure, the orthonormal basis of the interference vector space for the aperture position i is derived from $\mathbf{B_j}$. Let $\mathbf{G_i}$ be this orthonormal basis at position i. The radar record at this aperture position i is projected into this vector space to find the amplitude of each interference component contained in the signal as follow.

$$\underline{G_i} = [\ \underline{G_{i\ 1}}, \underline{G_{i\ 2}}, \underline{G_{i\ 3}}, \ \underline{G_{i\ 4}}],$$

$$A_i = [\ \underline{S_i}\ .\ \underline{\mathbf{G}_{i1}}, S_i\ .\ \underline{G_{i2}}, S_i\ .\ \underline{G_{i3}}, \ S_i\ .\ \underline{G_{i4}}], \tag{6}$$

The vector A_i represents the amplitudes of interference components contained in signal S_i. These unwanted components are removed from the radar record as follow.

$$\underline{\mathbf{S'}_i} = \underline{\mathbf{S}_i} - (\ A_{i1} * \underline{\mathbf{G}_{i1}} + A_{i2} * \underline{\mathbf{G}_{i2}} + A_{i3} * \underline{\mathbf{G}_{i3}} + A_{i4} * \underline{\mathbf{G}_{i4}} \tag{7}$$

Figure 21 shows the block diagram of the self-interference algorithm.

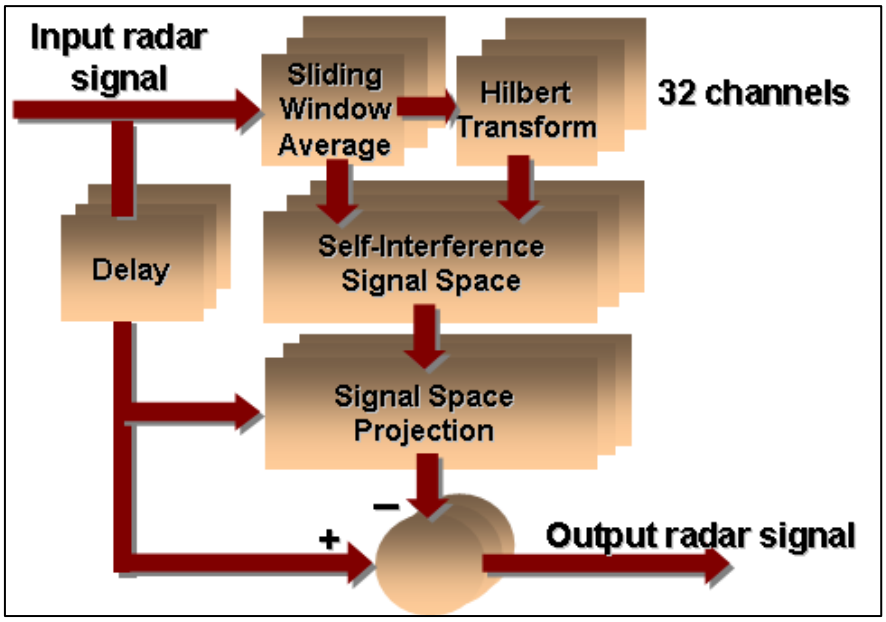

Figure 21. Block diagram of the self-interference algorithm.

Figure 22 shows the visualization for the data in figure 20 after applying the self-interference extraction algorithm. Note that the self-interference signals are significantly suppressed. The target signatures are no longer embedded in the self-interference signals; they form distinct traces with amplitudes that are well above the background level.

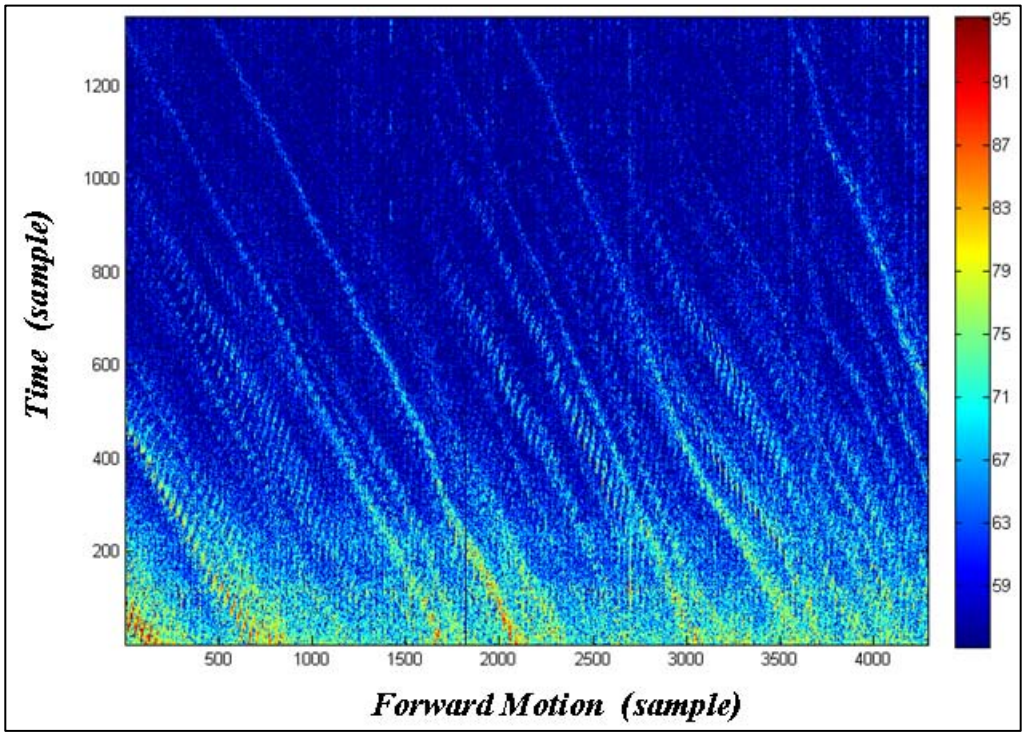

Figure 22. Visualization for the data in figure 20 after the application of the self-interference extraction algorithm.

Figure 23 shows the time-domain magnitude plots of a single radar range profile before and after the application of the self-interference removal algorithm. In this case, the average energy of the radar record is reduced by 20 dB. Although the suppression of the self-interference noise is significant, we want to know if there is any side effect on the targets. Figure 24 shows the time-domain signature plot of a target before and after the application of the self-interference removal algorithm. The target signature (range gates 165–175) is virtually unchanged after the application of the algorithm.

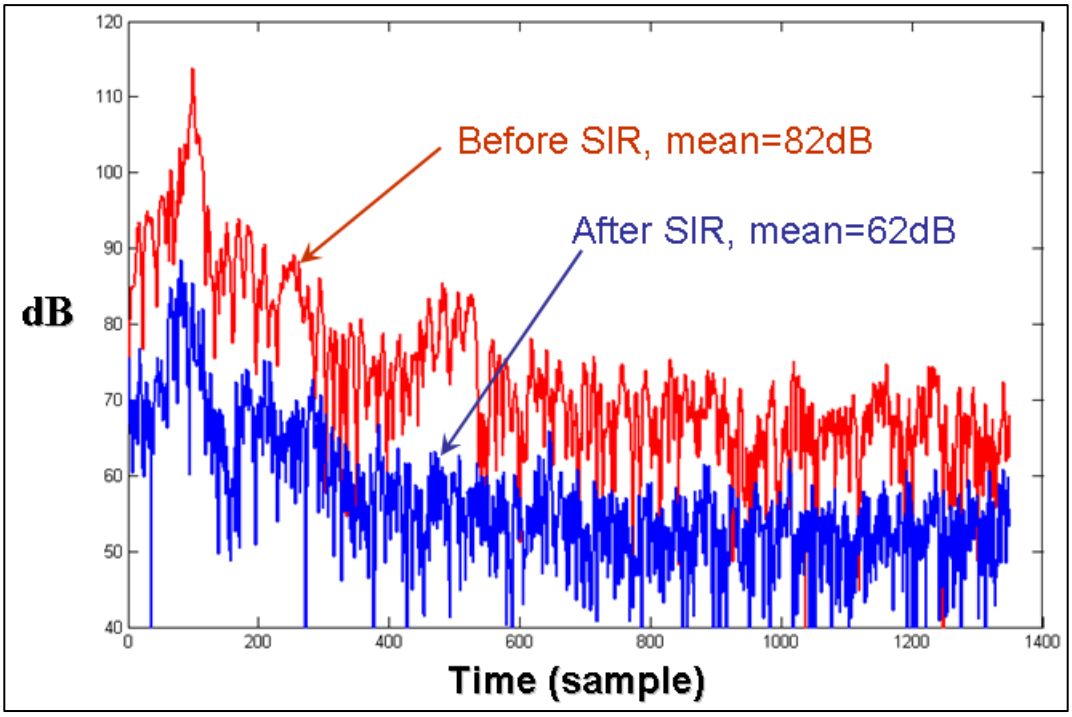

Figure 23. Time-domain magnitude plots of a single radar range profile before and after the application of the self-interference removal algorithm. In this case, the average energy of the radar record is reduced by 20 dB.

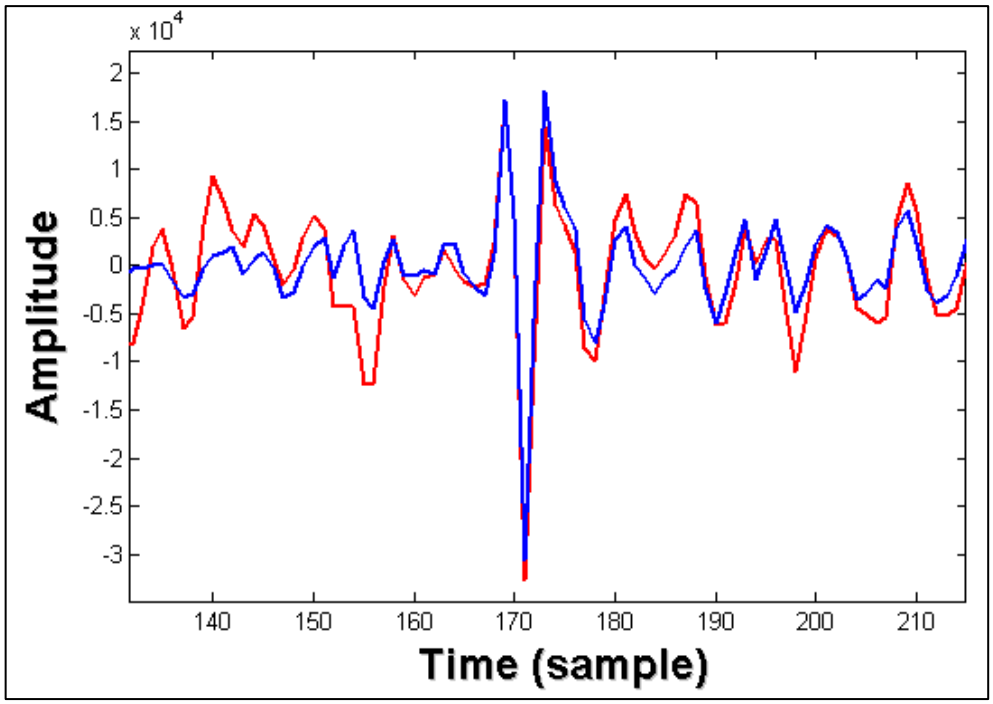

Figure 24. Time-domain signature plot of a target before and after the application of the self-interference removal algorithm. The target signature (range gates 165–175) is virtually unchanged after the application of the algorithm.

3.4 Data Processing to Remove Distortion due to the Radar Motion

There are two side effects that the SIRE sampling technique generates. The first one is discussed in section 3.2. In this section, we examine the second side effect, which is the distortion in phase and shape of the target signature when the radar is in motion. As mentioned previously, the advantage of the SIRE sampling technique (or other *equivalent-time* sampling techniques) is that it relieves the speed requirements for the ADC converters. However, the data acquisition time for signal reconstruction increases. If the radar is stationary during this data acquisition cycle, the radar signal will be perfectly reconstructed from the returned impulses. However, this assumption is not true since the relative position between the radar and the targets are no longer negligible during the data acquisition cycle due to the motion of the radar platform. This is especially true for forward-looking radar since the radar moves toward the imaging area. This relative motion between the radar and the targets during the data acquisition cycle results in severe phase and shape distortions in the reconstructed signal. This, in turn, results in poor focus quality and a low signal-to-noise level in SAR imagery. An algorithm has been developed to remove the severe phase and shape distortions of the target signatures in the reconstructed signal (*10*). Some results are highlighted here.

Let us consider a simulation case. The radar is located 15 m away from a point target and moving toward the target at the speed of 5 mph. The radar transmits impulse signals to the point target. The receiver performs the data acquisition on returned signals using the sampling

technique described in a previous section. After $M \cdot K$ (1024×193) pulses are transmitted and received, the data acquisition cycle is completed and the radar waveform is reconstructed. In figure 25, we show the reconstructed waveform of the moving case (red color) versus the ideal stationary case (blue color). In the time domain plot of figure 25a, the waveform from the stationary case represents the perfect reconstruction. On the other hand, the reconstructed waveform of the moving case (red) consists of two separated parts: the first part is similar (but with time compression) to the reconstructed waveform of the stationary case (blue) but with a significant *phase shift*, and the second part is a completely distorted pulse and is almost time-aligned with the ideal stationary case. Figure 25b show the distorted frequency spectrum of the moving reconstructed waveform versus that of the perfect case (stationary). The amount of phase and shape distortions of the reconstructed waveform depends on the speed of the radar platform, and the distance from the radar to the target.

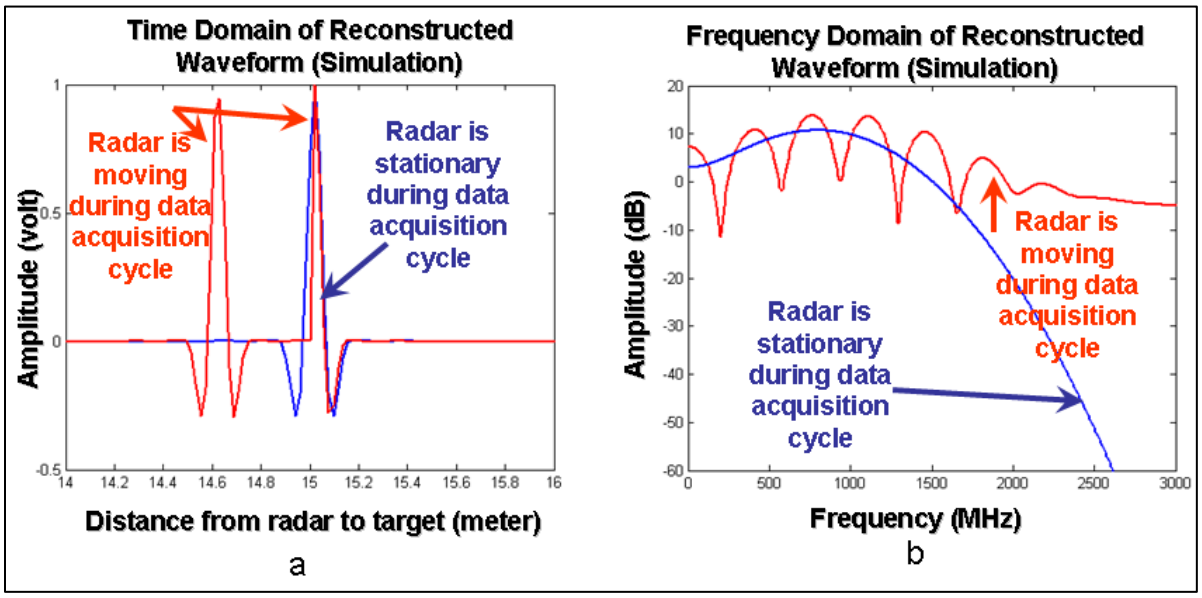

Figure 25. The reconstructed waveform of the moving case (red color) versus the ideal stationary case (blue color) in (a) time domain, and (b) frequency domain.

Figure 26 shows the false color plot of seven frames of radar signatures from an 8-ft trihedral measured by the SIRE radar as it moves at the speed of 5 mph. Each frame of data consists of 16 received waveforms from 16 receivers. In each data frame, we should expect two responses: (1) the first large response from the trihedral and (2) a much weaker response due to the transmitter artifact. Similar to the simulation case, we can notice the obvious shape distortion occurred in frames 1, 2, 4, and 6. In frames 2 and 6, the main responses split while in frames 1 and 4, the secondary responses split.

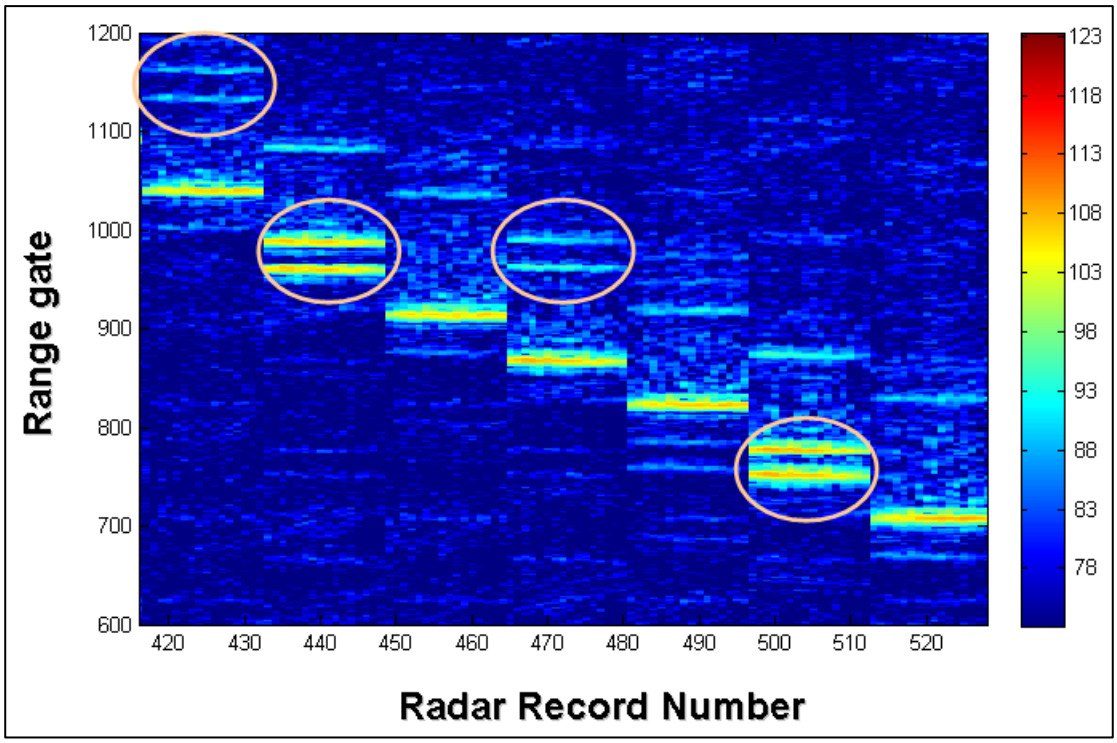

Figure 26. Data visualization for seven frames of radar signatures from an 8-ft trihedral measured by the SIRE radar as it moves at the speed of 5 mph.

The phase and shape distortions in the reconstructed waveform can be explained as follow. Figure 27 shows the data reconstruction scheme when the radar is moving during the data acquisition cycle. For the reconstructed waveform, the effective sampling period is

$$\Delta_m = \Delta + \frac{2v \cdot M \cdot PRI}{c}, \tag{8}$$

which is no longer has the same value as Δ in figure 9. In equation 8, v is the speed of the radar during this acquisition group of M pulses. From equation 8, the effective sampling period for the reconstructed waveform is varied with the radar instantaneous speed. This generates the phase and shape distortion in the reconstructed waveform. Another source of artifact in the reconstructed waveform is depicted in figure 27. The last samples of the first range (measured at the slower A/D rate) overlap with the beginning samples of the second range gate. This creates the spurious glitches in the reconstructed waveforms (shown in figure 25a). From equation 8, we assume that the radar speed v is constant during the entire data acquisition cycle. This is not a bad assumption since the radar is moving slowly and its speed should not change too much during the period of 197 ms.

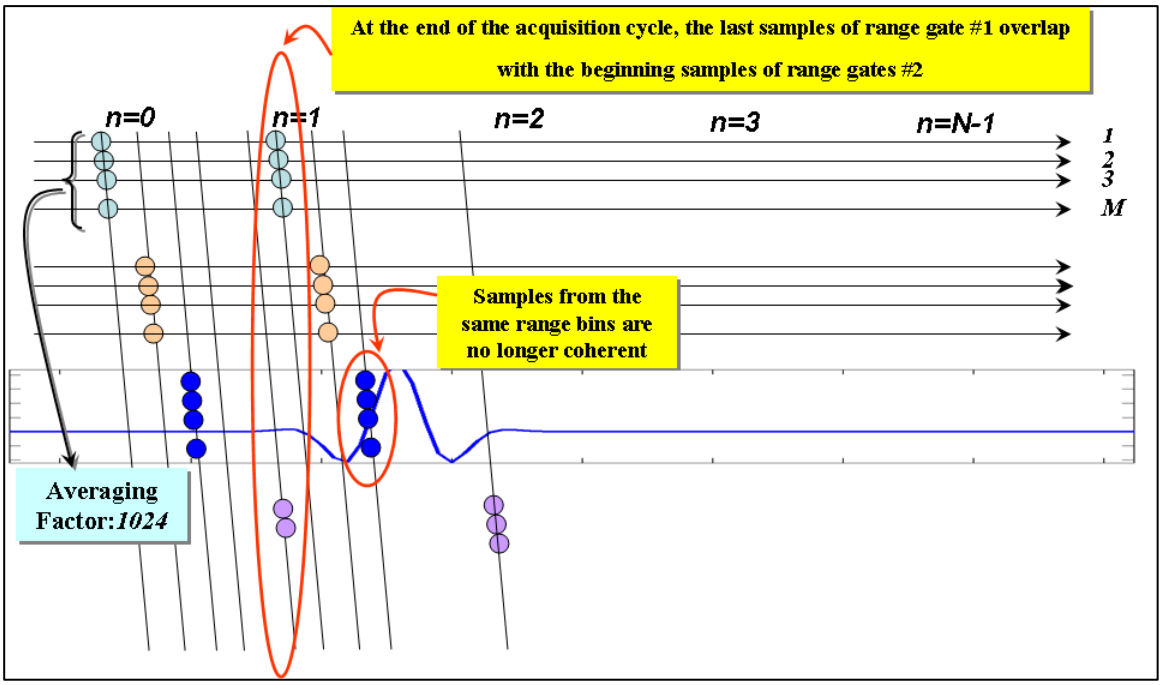

Figure 27. Data reconstruction scheme when the radar is moving during the data acquisition cycle.

The algorithm for the removal the side-effect due to the radar motion is described in reference 10.

We applied the forward motion processing algorithm to the data of an 8-ft trihedral (figure 26). In each data frame of figure 26, we should expect two responses: (1) the first large response from the trihedral and (2) a much weaker response due to the transmitter artifact. However, we can notice the obvious shape distortion occurred in frames 1, 2, 4, and 6. In frames 2 and 6, the main responses split while in frames 1 and 4, the secondary responses split. In addition to the shape distortion, the phase errors are also present. Figure 28 shows the data after processing. Notice that the both the phase and shape distortions of the trihedral signatures are corrected in figure 28.

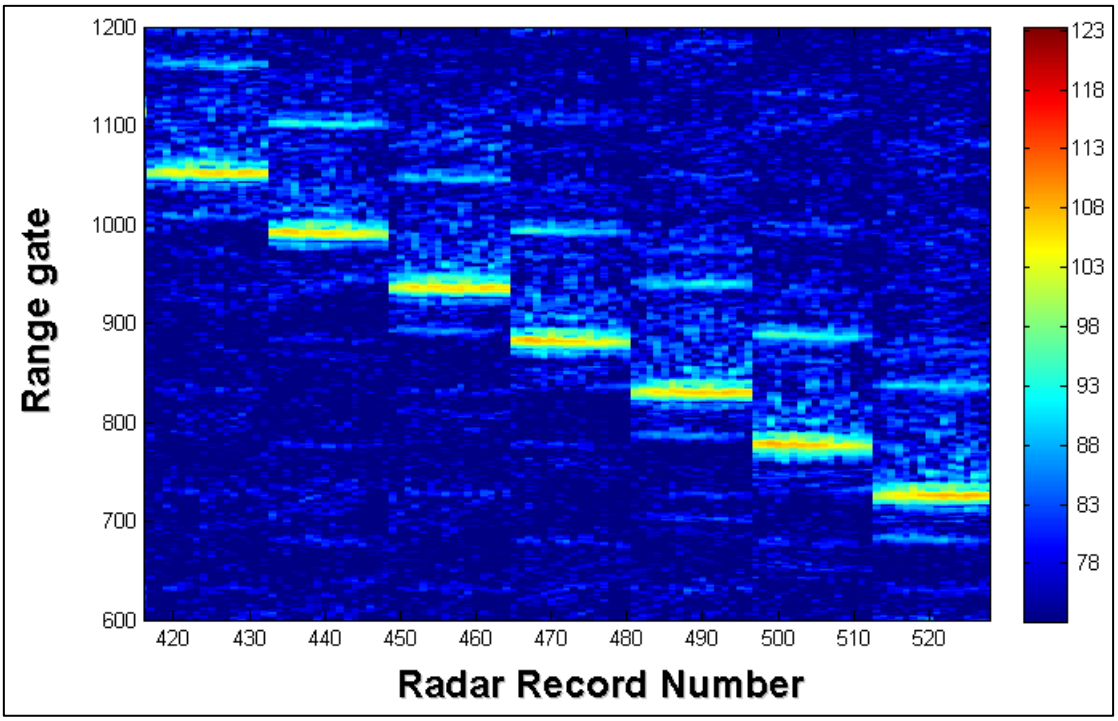

Figure 28. Data visualization (after forward motion processing) for seven frames of radar signatures from an 8-ft trihedral measured by the SIRE radar as it moves at the speed of 5 mph.

3.5 Backprojection Image Formation

3.5.1 Backprojection Image Formation Concept

After all the signal processing steps are applied to the returned radar signals, the processed radar range profiles may be used for forming a SAR image. Over the last decade, ARL has been using the backprojection image formation (*11*) for various applications (*12–14*). Figure 29 illustrates an example using the basic concept of the backprojection imaging algorithm. The radar is mounted on a moving platform. It transmits radar signals to illuminate the area of interest and receives return signals from the area. Using the motion of the platform, the radar collects K data records along its path (or aperture). In general, the aperture could be a line, a curve, a circle, or any arbitrary shape. The receiving element k from the aperture is located at the coordinate $(x_R(k), y_R(k), z_R(k))$. For bistatic radar (the transmitting antenna is separate from the receiving antenna), the transmitting element k from the aperture is located at the coordinate $(x_T(k), y_T(k), z_T(k))$. For monostatic radar (the transmitting antenna is the same as or co-located with the receiving antenna), the transmitting coordinates $(x_T(k), y_T(k), z_T(k))$ would be the same as the receiving coordinates $(x_R(k), y_R(k), z_R(k))$. Since the monostatic radar case is a special case of the bistatic radar configuration, the algorithm described here is applicable for both configurations. The returned radar signal at this receiving element k is $s_k(t)$. In order to form an image from the area of interest, we form an imaging grid that consists of N image pixels. Each pixel P_i from the imaging grid is located at coordinate $(x_P(i), y_P(i), z_P(i))$. The imaging grid is

usually defined as a 2-D rectangular shape. In general, however, the image grid could be arbitrary. For example, a three-dimensional (3-D) imaging grid would be formed for ground penetration radar to detect targets and structures buried underground. Another example is 3-D image of the human body inside. Each measured range profile $s_k(t)$ is corrected for the $\frac{1}{R^2}$ propagation loss, i.e., $s_k'(t) = R^2(t)s_k(t)$, where $R(t) = \frac{ct}{2}$ and $c = 2.997e^8 m/\sec$. The backprojection value at pixel $P(i)$ is

$$P(i) = \sum_{k=1}^{K} w_k s_k'(f(i,k)), \qquad 1 \le i \le N \tag{9}$$

where w_k is the weight factor and $f(i,k)$ is the delay index to $s_k'(t)$ necessary to coherently integrate the value for pixel $P(i)$ from the measured data at receiving element k.

The index is computed using the round-trip distance between the transmitting element, the image (pixel), and the receiving element. The transmitting element is located at the coordinate $(x_T(k), y_T(k), z_T(k))$. The distance between the transmitting element and the image pixel $P(i)$ is

$$d_1(i,k) = \sqrt{[(x_T(k) - x_P(i))]^2 + [(y_T(k) - y_P(i))]^2 + [(z_T(k) - z_P(i))]^2} \tag{10}$$

The distance between the receiving element and the image pixel $P(i)$ is

$$d_2(i,k) = \sqrt{[(x_R(k) - x_P(i))]^2 + [(y_R(k) - y_P(i))]^2 + [(z_R(k) - z_P(i))]^2} \tag{11}$$

The total distance is

$$d(i,k) = d_1(i,k) + d_2(i,k) \tag{12}$$

The delay index is

$$f(i,k) = \frac{d(i,k)}{c} \tag{13}$$

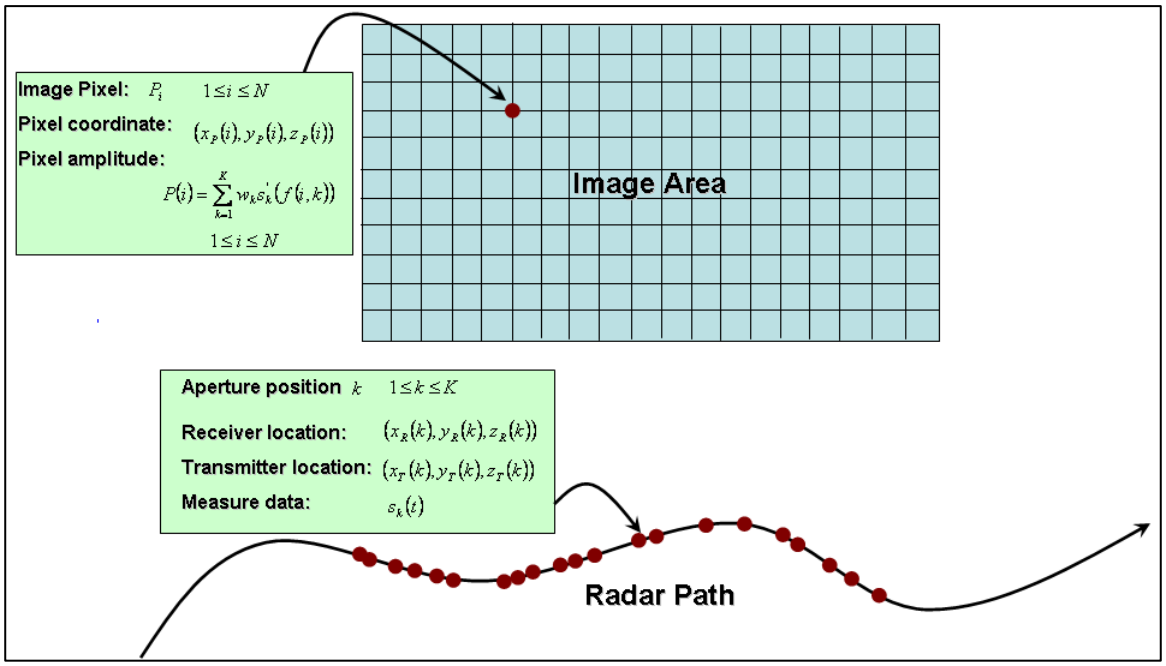

Figure 29. Backprojection image formation.

3.5.2 Forward-looking Image Formation Using Backprojection and Mosaicking Technique

Figure 30 shows the forward-looking imaging geometry employed by the SIRE radar. The radar transmits wideband impulses to an area in front of the vehicle using the left transmit antenna. The backscatter radar signals are captured by the physical array of 16 receive antennas and 16 receivers. The radar then switches to the right transmit antenna to continue the process. The SAR image in figure 30 (right) shows the result of the backprojection algorithm applied to 32 radar data records (16 data records received using the left transmitter and 16 data records received using the right transmitter). In this simulation case, there are five point targets within the imaging area and other targets that are out of the imaging area. These out-of-scene targets represent the clutter objects that exist in real life such as trees, bushes, and other manmade objects. As we can see from the resulting SAR image, although the five point targets can be easily detected, the sidelobes from these point targets and especially from the out-of-scene targets are quite high. These sidelobes form a noise floor in the SAR image and make it difficult to detect targets with a lower RCS. Figure 31 shows that in addition to the physical array of 16 receivers, the forward motion of the vehicle introduces another dimension. Combining both the physical dimension and the motion dimension, we can form a 2-D aperture for forming image. Figure 31 (right) shows the SAR image using the same target setup as in figure 30, except that the backprojection algorithm performs the image formation using the 2-D aperture. We can see the sidelobes from this SAR image (figure 31) are significantly reduced compared to the SAR image of figure 30. Because of the change in geometry when the vehicle is moving forward, the targets can be better resolved and the sidelobes are significantly reduced.

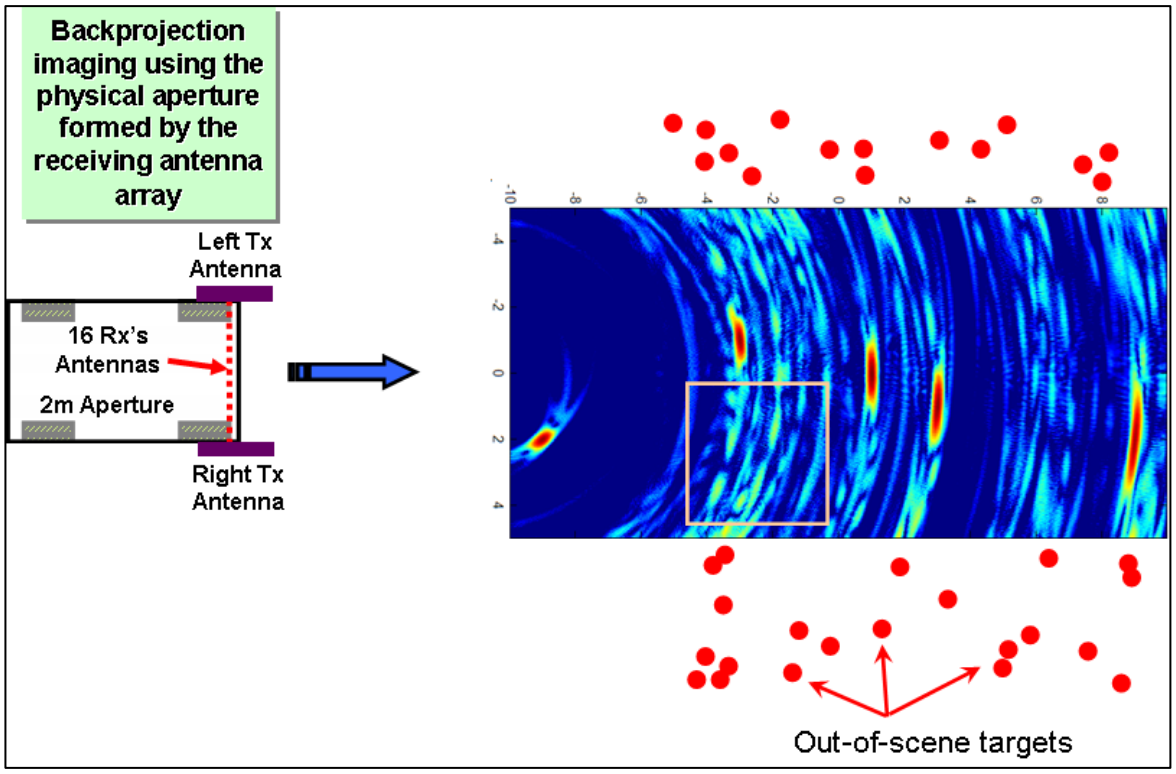

Figure 30. Forward-looking imaging geometry employed by the SIRE radar. The SAR image (right) shows the result of the backprojection algorithm applied to 32 radar data records (16 data records received using the left transmitter and 16 data records received using the right transmitter).

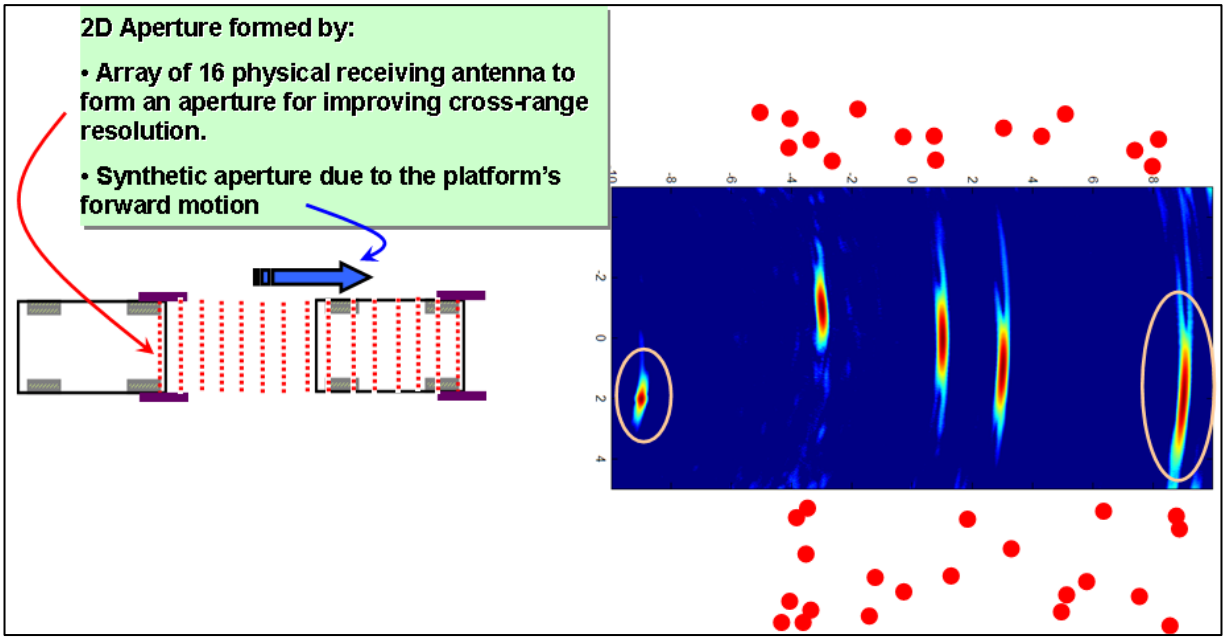

Figure 31. 2-D aperture is formed by combining both the physical dimension and the motion dimension. The SAR image (right) with the same target setup as in figure 30, except that the backprojection algorithm performs the image formation using the 2-D aperture.

Although we have achieved a much better SAR image by combining the physical array of receiving elements and the forward motion of the vehicle, the near-range target (first target from figure 31) is much more compact compared to the far-range target (fifth target). In other words, the near-range image pixels have better resolution than far-range image pixels. The reason is that the total integration angle of the radar aperture for the near-range pixels is higher than that for the far-range pixels.

To overcome this problem, we implement the following mosaic approach, as illustrated in figure 32. The following is a description of the platform in figure 32 as it passes four sequential positions A, B, C, and D located along the *x*-axis. The formation of the first sub-image begins when the platform is at the coordinate A, with a distance X_0 (the typical value is 20 m) from the center of the first sub-image. As the platform travels in the *x* direction, the radar continues the operation to illuminate the imaging area, acquire the backscatter data, and perform the image formation. The formation of the first sub-image ends when the platform reaches coordinate C, with a distance X_1 (the typical value is 8 m) from the center of the first sub-image. Accordingly, the radar signal data for the first (full-resolution) sub-image is received as the radar platform travels a distance of $X_0 - X_1$ (20 m – 8 m = 12 m in our example) from coordinates A to C, for formation of a 2-D aperture. The distance traveled during the formation of the 2-D aperture is represented by an arrow in figure 32 labeled “Aperture 1.” The along-track dimension of each sub-image is assigned to be small to avoid a significant change in resolution from the near-range pixels to the far-range pixels as illustrated in figure 31. The typical value of the along-track dimension of each sub-image used by the SIR radar is 2 m.

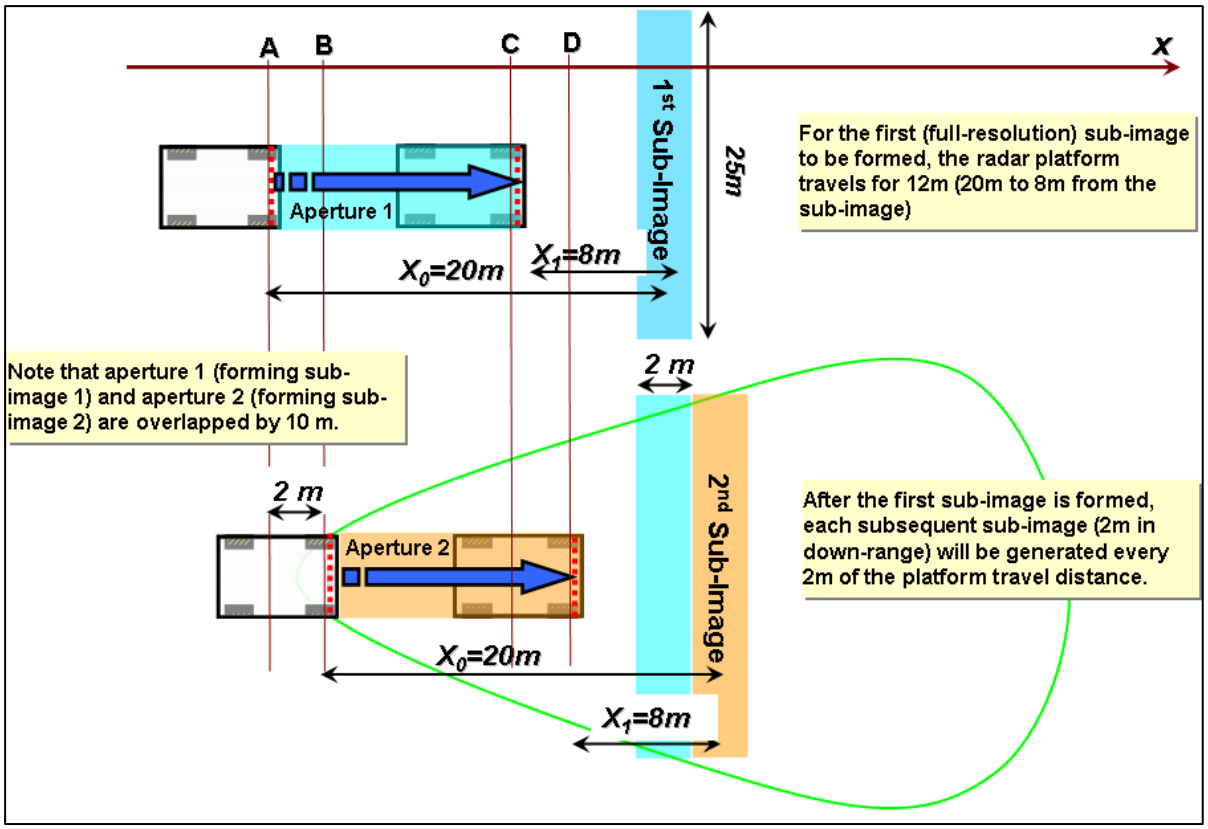

Figure 32. Mosaic approach for forward-looking imaging to have consistent resolution across the image.

When the platform reaches coordinate B, a distance of 2 m—which is also the along-track dimension of each sub-image—from coordinate A in figure 32, the formation of the second sub-image begins, and as the platform travels to coordinate D, it uses the received data to form a second 2-D aperture. The distance traveled by the platform is represented by an arrow in figure 32 labeled "Aperture 2." Note that the two apertures are overlapped by 10 m and the second aperture is "advanced" by 2 m with respect to the first aperture. Sub-images 1 and 2 are formed from the 2-D apertures using the same length of travel (12 m) of the radar. This process is applied to ensure that image pixels have almost the same (within a specified tolerance) resolution across the entire large area. The sub-images are formed from the radar range profiles using the backprojection algorithm.

Figure 33 shows the backprojection algorithm applied to form a sub-image. The procedure mathematically described with respect to figure 29 in the previous paragraphs may also be applied to this imaging scenario. In this case, the radar aperture is a rectangular array that is formed by an array of 16 receiving elements (that spans 2 m) and the forward motion of the platform (12 m for forming each sub-image). The imaging grid in this case is defined as a rectangular array of 25 by 2 m.

Figure 34 shows the integration range as a function of cross-range pixel in the image. Our current integration strategy is to integrate from 8 m to 20 m. This is true for the center pixels (0 m in the *x*-axis). As the image pixels move off to the side, both the lower limit and upper limit of the integration range increase.

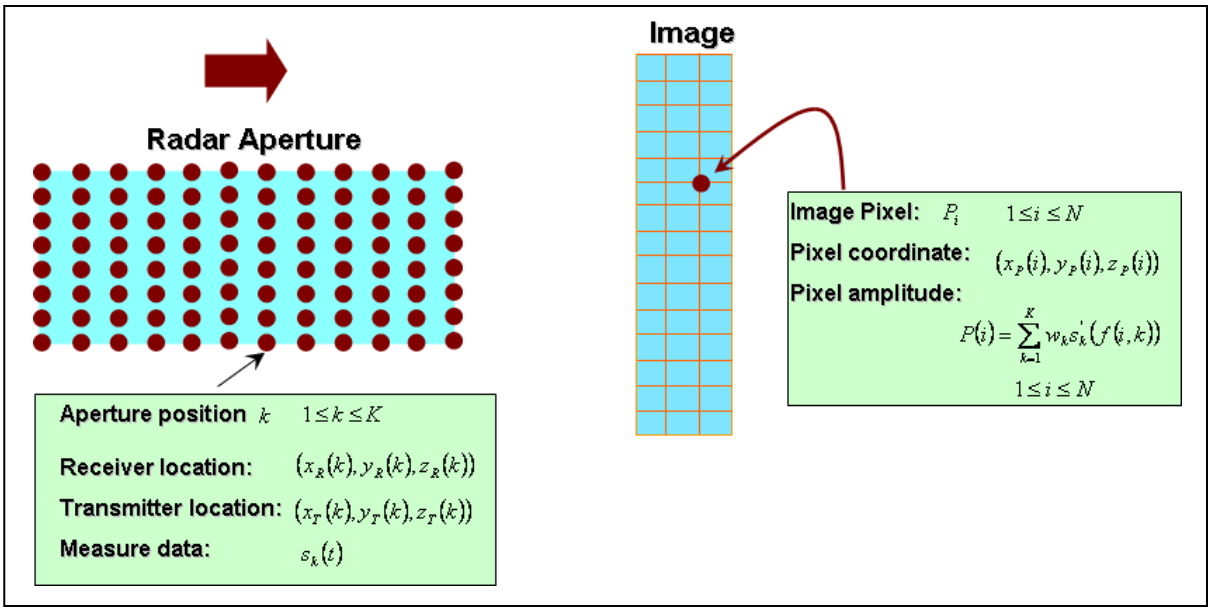

Figure 33. Backprojection algorithm applied to form a sub-image.

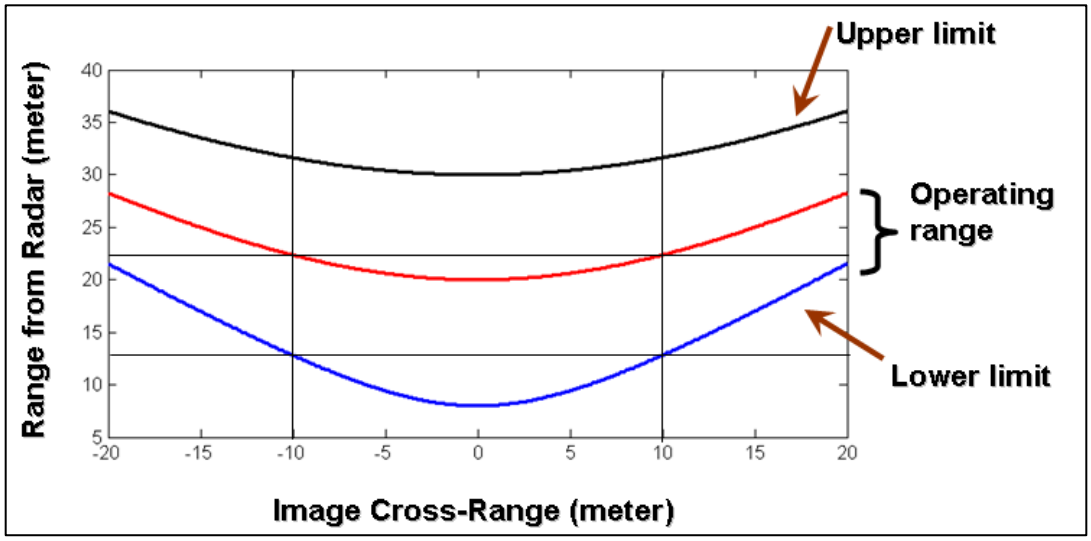

Figure 34. Integration range as a function of cross-range pixel in the image.

3.5.3 Sample Forward-looking SAR Images from SIRE Radar and the Challenge of the Multiplicative Noise

Figure 35 shows two segments of SAR imagery formed using measured data from the SIRE radar in forward-looking mode. Each image segment covers an area of 25 m in the cross-track direction and 64 m in the along-track direction. Both are displayed using a wide dynamic range (40 dB). Overall, the image quality is good. Targets are well focused and the image contrast is very good. However, these images show that multiplicative noise is a big problem. Multiplicative noise is much more difficult than additive noise to deal with since it is data dependent. Some sources that cause multiplicative noise include timing jitter in data sampling, small aperture size compared to image area, the under-sampling of aperture samples, the non-uniform spacing between aperture samples, and errors in the position measurement system. Multiplicative noise results in undesired sidelobes that create a high noise floor in the image and thus limit the ability to detect targets with smaller amplitudes. From figure 35, sidelobes from manmade objects and natural clutter, and reflected energy from large RCS objects, spread throughout the image and thus raise the noise background level of the image. The level of this noise floor is proportional to the number of manmade and natural clutter objects, especially the ones with a large RCS. This is a big challenge for the detection of targets with a smaller RCS, which might be obscured or even embedded in the multiplicative noise floor. In the next section, we describe the recently developed algorithm to suppress this type of noise from SAR imagery.

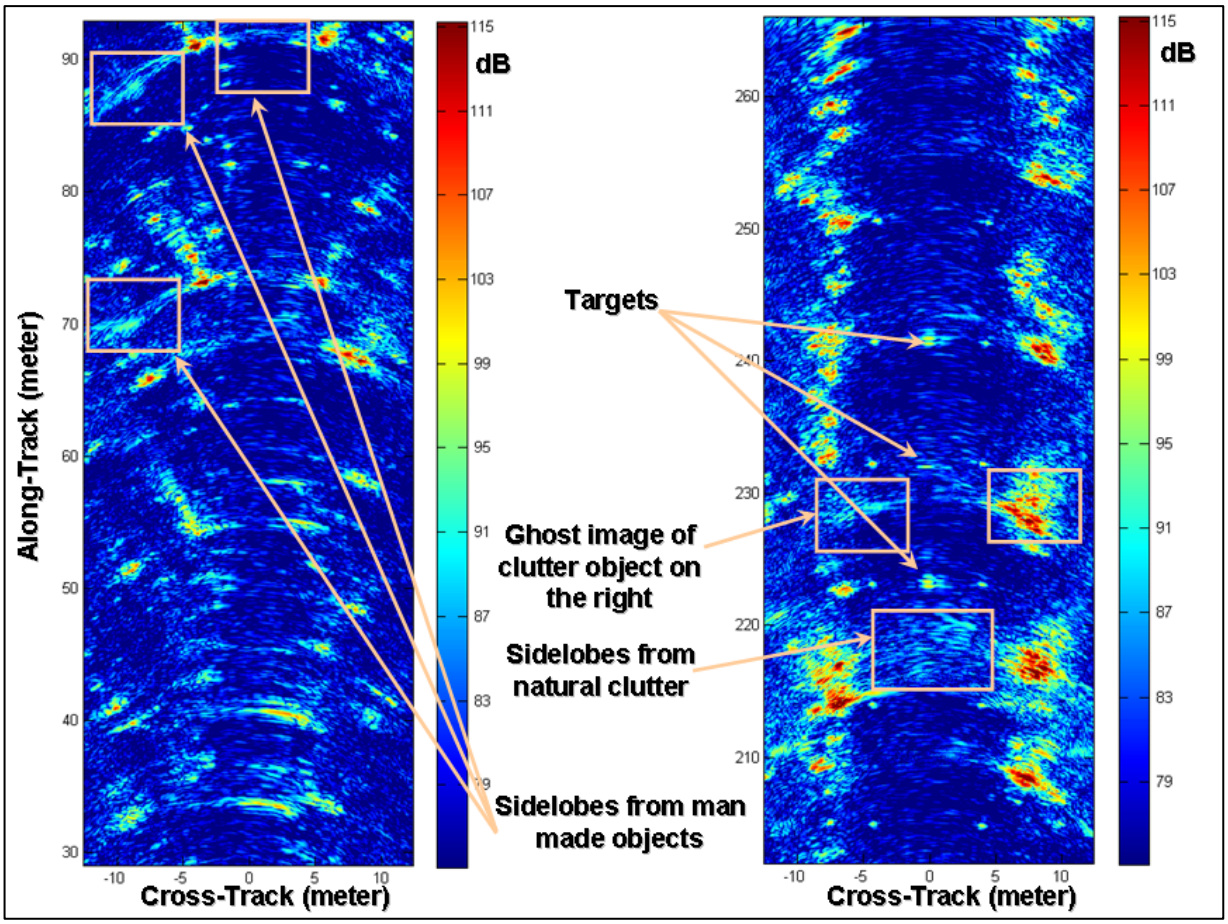

Figure 35. Two segments of SAR imagery formed using measured data from the SIRE radar in forward-looking mode.

3.6 Recursive Sidelobe Minimization (RSM) Technique

In this section, we present the (patent pending) RSM technique (*15*), which is designed to suppress sidelobes and noise from SAR imagery.

First, we developed some the simulation cases to understand the causes of the multiplicative noise from SAR imagery and developed a technique to suppress it. Figure 36 shows a SAR image formed using the above algorithm and simulated data of two point targets. The image is displayed using 40 dB of dynamic range. However, “energy” from the two point targets is spread throughout the image and creates severe sidelobes. The two sources that generate the imaging artifacts in this case are (1) aperture aliasing (small aperture compared to the large image cross-range swath) and (2) the errors from the position measurement system. In reality, there are many other sources that contribute to the noise floor of the resulting image. This created a challenging problem for the detection of targets of smaller amplitudes since they might be obscured or even embedded in the noise floor.

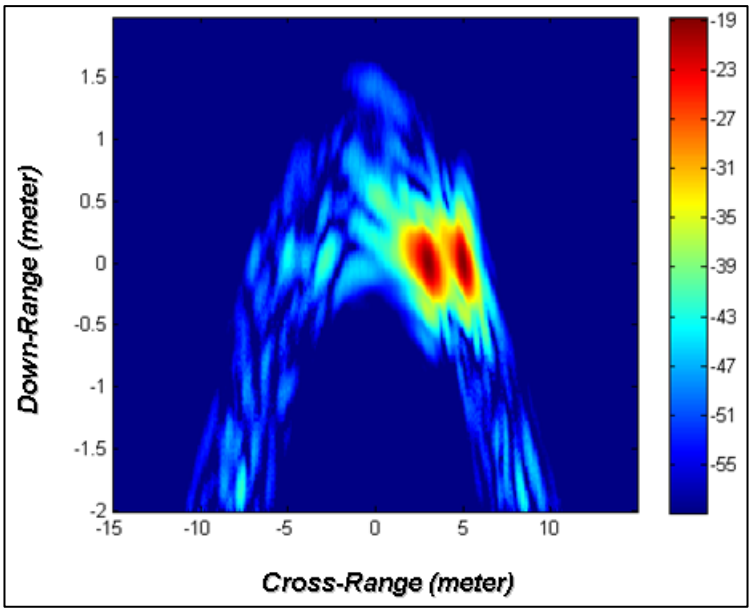

Figure 36. SAR image formed using the simulated data of two point targets. The two sources that generate the imaging artifacts are in this case (1) the aperture aliasing (small aperture compared to the large image cross-range swath) and (2) the errors from the position measurement system.

In conventional signal processing techniques, we usually avoid non-uniform and sparse data. From basic digital signal processing theory, it is well-known that if a gap is introduced in the time-domain (missing data points), the corresponding frequency spectrum would suffer from the large resulting sidelobes. The reverse is also true: any gap (missing data points) in the frequency domain would result in severe sidelobes in the corresponding time-domain. For SAR processing, we also encounter situations where we have to work with sparse (incomplete) data. One approach for improving SAR image in such situations is to estimate and fill in the missing data samples in the aperture data domain (*16*).

For the SAR image of figure 36, although we start with uniform and complete data in the aperture domain, the resulting SAR image suffers from severe sidelobes due to two sources described previously. Since the radar data in the aperture domain are uniform and complete, we wanted to see what would happened if we randomly removed a number of samples from the aperture. Figure 37 (left) shows the complete aperture and the corresponding SAR image. Figure 37 (right) shows the *compressive aperture* with a number of samples removed and the corresponding SAR image. As expected, the SAR image with a number of aperture data samples removed has much larger sidelobes than that using the data from the complete aperture. Generally speaking, it is not intuitive as to why only a subset of the original radar aperture would be used instead of the full aperture for forming an image, since the gaps introduced in the subset of an aperture would seem to result in inferior performance. As mentioned previously, in conventional techniques, one always prefers the full data set and avoids the gapped data set. However, the benefit of this compressive approach is examined next.

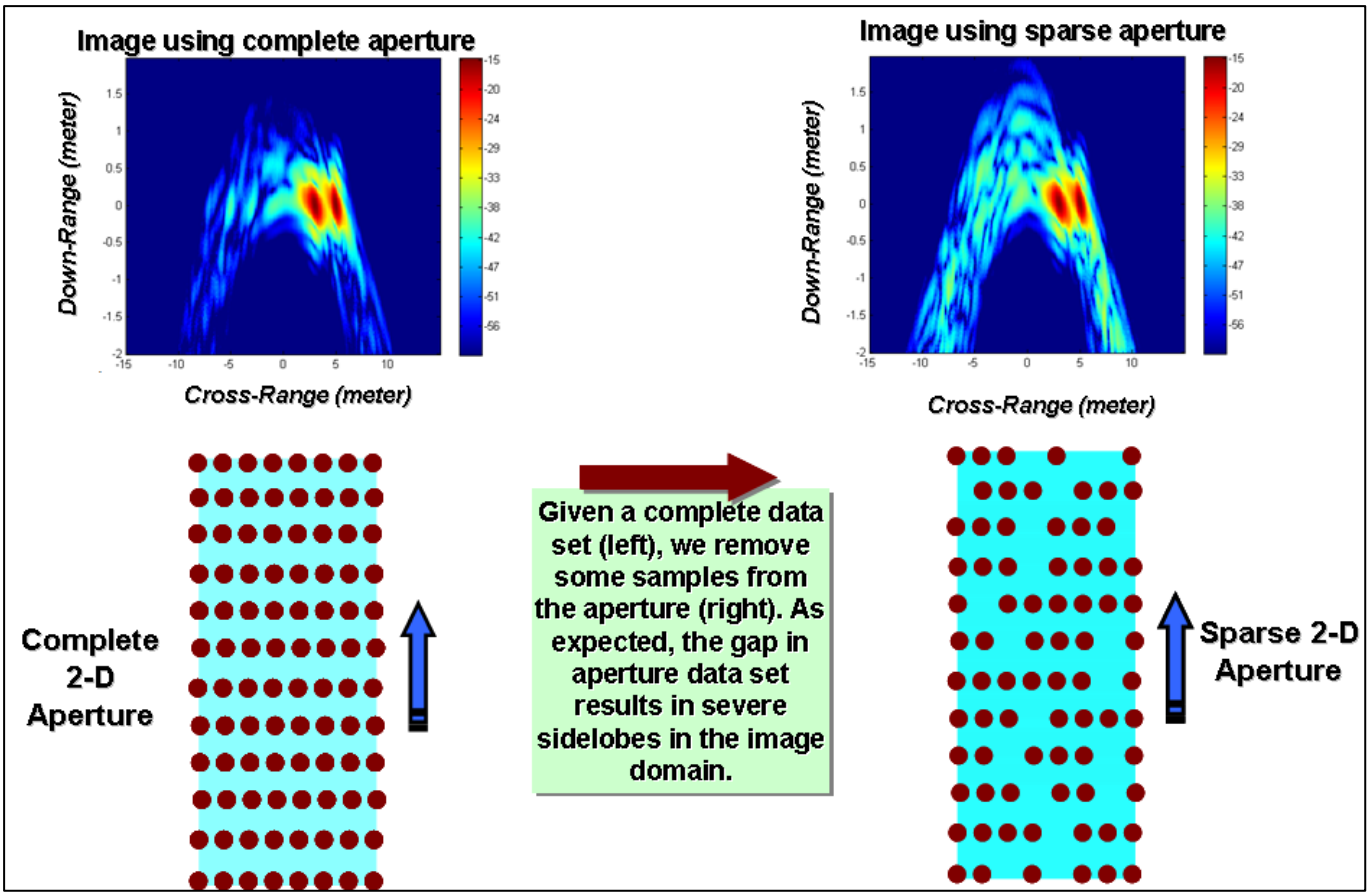

Figure 37. (Left) Complete aperture and the corresponding SAR image and (right) c*ompressive aperture* with a number of samples removed and the corresponding SAR image.

We repeat the process of randomly removing a number of samples from the original complete aperture. Since the selection of samples to be removed is randomized, the gap (missing data) pattern would be different than the previous realization. Figure 38 shows the two SAR images formed using two incomplete apertures (with removed data samples).

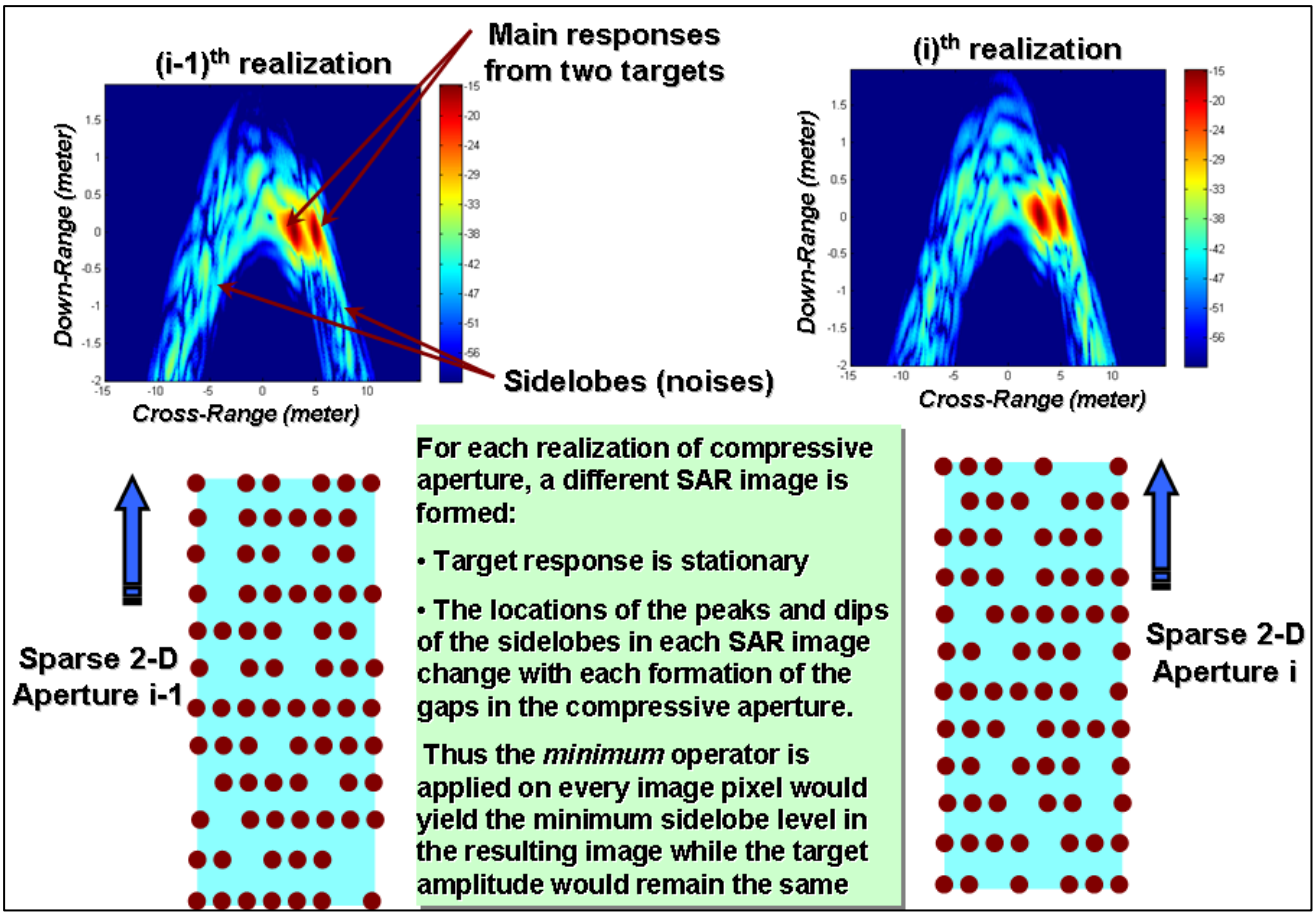

Figure 38. Two SAR images formed using two incomplete apertures (with removed data samples).

We want to emphasize the following two important factors. First, since the main responses from the targets are coherently integrated and normalized by the image formation process, the locations and the peak values of the targets in the resulting SAR images (figure 38) are the same. Second, the locations and amplitudes of peaks and valleys of the sidelobes change with each formation of the gaps in the compressive aperture. The reason is that the only pixel location in the SAR image that is coherently integrated is the target location. Other pixel locations (with sidelobes) are incoherently integrated and thus the values and the locations change with each realization of compressive aperture. Thus, applying the *minimizing* operator on every image pixel pair from the two resulting compressive SAR images would yield the minimum sidelobe level in the resulting image, while the target amplitudes would remain the same. Figure 39c shows the result after the *minimizing* operator is applied to both SAR images of figures 39a and 39b. Note that the sidelobes of the resulting image are lower than that from either of the original SAR images because of the random locations of the peaks and dips of the sidelobes from each image. On the other hand, the amplitudes of the resulting targets remain the same.

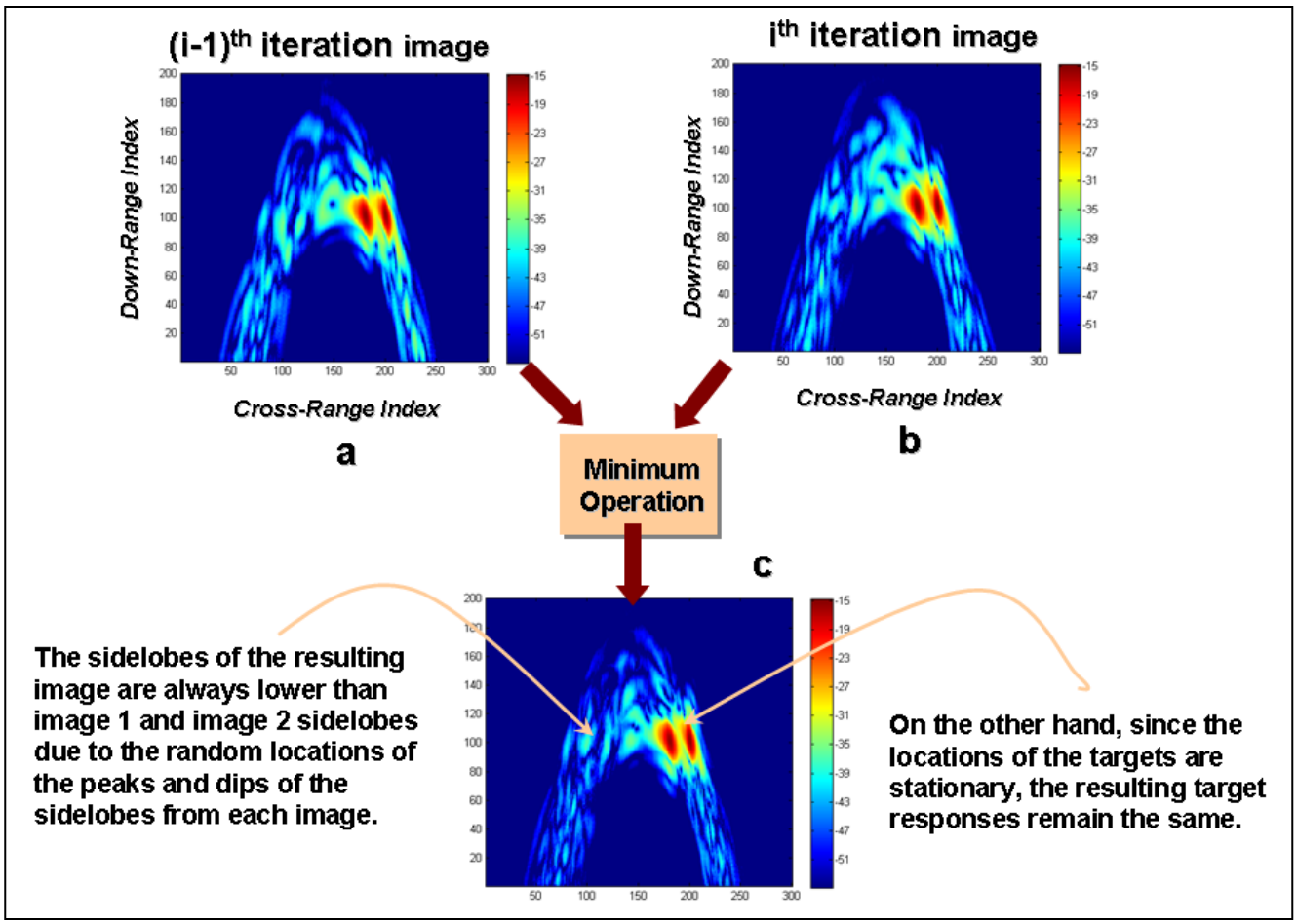

Figure 39. (c) Result after the *minimizing* operator is applied to both SAR images of (a) and (b).

Figure 40 shows a comparison of the cross-range profiles from the two compressive SAR images and the resulting minimization SAR image. As graphically presented in figure 40, the amplitudes of the resulting two targets remain the same after the *minimizing* operation. In addition, the locations of the targets do not change. However, the sidelobes of images 1 and 2 are diminished during the minimizing step due to the random location of the peaks and dips of the sidelobes from each image. Many realizations of compressive aperture are generated, each with a different gap pattern. Due to the randomness of the locations of the peaks and valleys of the sidelobes, the combined SAR image using all of these realizations would have a very low sidelobe level.

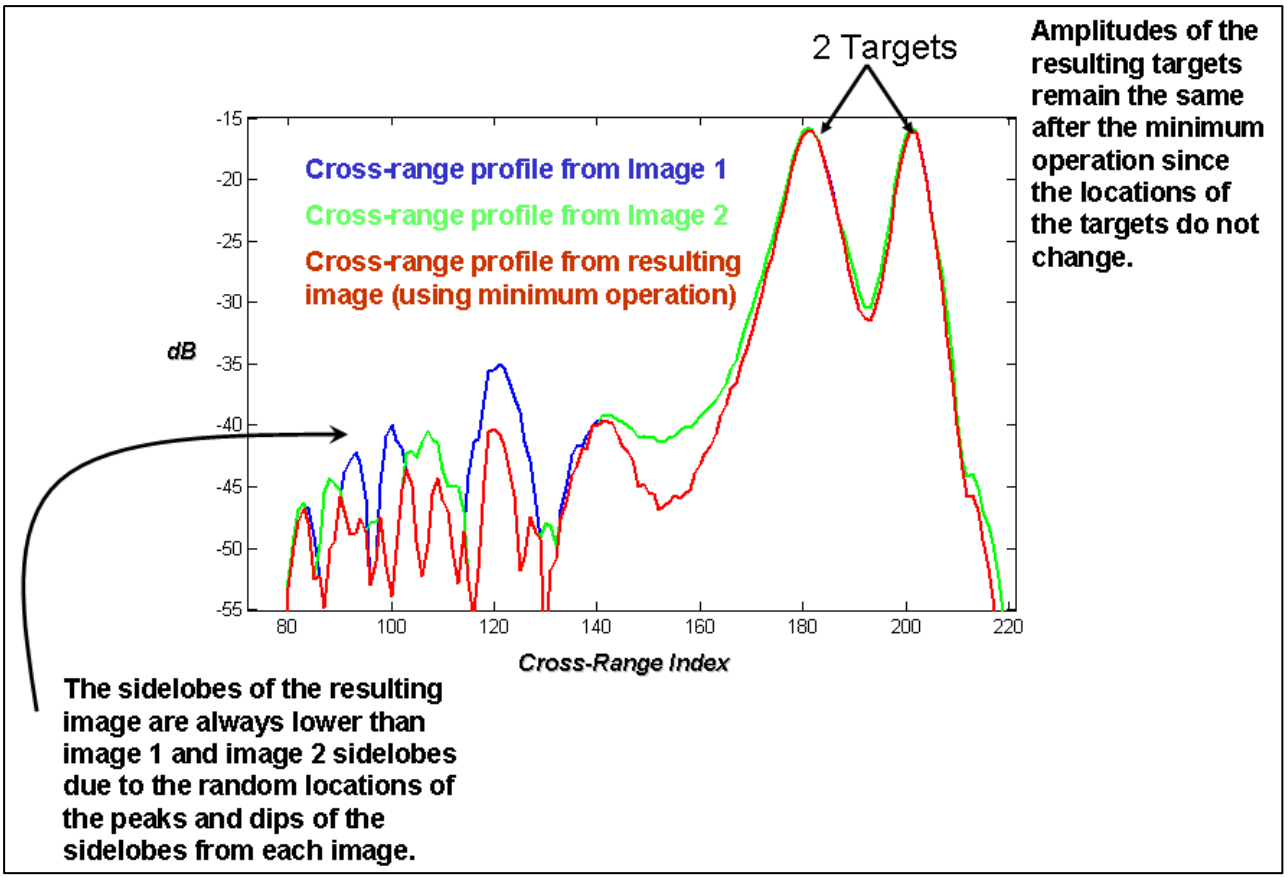

Figure 40. Amplitudes of the resulting two targets remain the same after the *minimizing* operation. The locations of the targets do not change; however, the sidelobes of images 1 and 2 are diminished during the minimizing step due to the random location of the peaks and dips of the sidelobes from each image.

This is the main concept of the RSM technique. The complete algorithm is described below.

Step 1

Radar data and its position information is acquired.

Step 2

The radar aperture is formed in preparation for image formation. The aperture consists of K elements. Each element in the radar aperture includes the radar receiving position information $(x_R(k), y_R(k), z_R(k))$, the radar transmitting information $(x_T(k), y_T(k), z_T(k))$, and the data record $s_k(t)$ that the radar measures at this location. For side-looking radar, the aperture is usually a linear path with data measured along the path. For the forward-looking radar mentioned previously, a 2-D radar aperture is generated, formed by the physical antenna array and the forward motion of the radar. In general, the radar aperture may take any of a variety of shapes.

Step 3

The imaging grid is formed. In this forward-looking implementation, a rectangular imaging grid is generated although the imaging grid could be arbitrary defined. Each pixel P_i in the imaging grid is located at coordinate $(x_P(i), y_P(i), z_P(i))$.

Step 4

A random compressive aperture is generated using the radar aperture with K elements from step 2. The compressive aperture is formed by selecting only L elements from the original aperture for the imaging process. The value for L is

$$L = p \cdot K \text{, where } 0 < p < 1 \tag{14}$$

Accordingly, only a subset of the aperture positions is used for image formation. The remaining $K - L$ aperture positions are simply discarded for this realization. The typical number that we use for our configuration is $p = 0.8$ (i.e., 80% of the aperture is employed and 20% of the aperture is discarded at each iteration). The value of p that can achieve the best result should be examined and optimized for each configuration of geometry and radar data set. The selection of L aperture positions is completely random for each realization. If A_l represents a vector that contains the indices of aperture positions to be included in the image formation process for l^{th} realization, then

$$A_l = \langle a_{l1}, a_{l2}, ..., a_{lL} \rangle \tag{15}$$

where a_{lm} is a random number, $1 \le a_{lm} \le K$ and $a_{lm} \ne a_{ln}$ for $m \ne n$. (16)

Step 5

The image is formed using the compressive aperture generated from step 4. The compressive aperture derived from A_l with L elements is then used to form the l^{th} realization of the sub-image using the backprojection method as described previously.

This results in the l^{th} realization of the sub-image with I pixels in the downrange direction and J pixels in the cross-range direction, where $N = I \cdot J$

$$I_l = \langle P_l(i) \rangle, \qquad 1 \le i \le N, \tag{17}$$

where $P_l(i)$ is computed using equation 9 with modification, reproduced below:

$$P(i) = \sum_{k \in A_l} w_k s_k'(f(i,k)) \tag{18}$$

Note that in the summation, the values of index k are selected from the random vector A_l defined in equation 15.

Step 6

The envelope of the image generated in step 5 is computed. The image generated in step 5 can also be written as

$$I_l = \left\langle P_{lj}(i) \right\rangle, \qquad 1 \le i \le I, \qquad 1 \le j \le J, \tag{19}$$

where P_{lj} is the j^{th} downrange profile from the l^{th} realization sub-image.

The corresponding quadrature component of this image downrange profile is computed by applying the Hilbert transform filter to the in-phase component:

$$PH_{lj} = Hilbert(PH_{lj}). \tag{20}$$

The Hilbert transform filter has magnitude 1 at all frequencies and introduces a phase shift of $-\frac{\pi}{2}$ for positive frequencies and $+\frac{\pi}{2}$ for negative frequencies. Thus, the Hilbert transform filter is used to shift the real signal (each image downrange profile) by $\frac{\pi}{2}$ to generate its quadrature component in order to compute its envelope.

The envelope of the j^{th} downrange profile from the l^{th} realization of the image may be computed as

$$PE_{lj} = \sqrt{\left(P_{lj}\right)^2 + \left(PH_{lj}\right)^2} \text{ (where the subscript is } lj\text{).} \tag{21}$$

The envelope of this image is simply

$$I_l = \left\langle PE_{lj}(i) \right\rangle, \qquad 1 \le i \le I, \qquad 1 \le j \le J. \tag{22}$$

Step 7

An intermediate resulting image is computed. The minimum operator is applied to two images: (1) the intermediate result from previous iteration $(l-1)^{th}$ and (2) the image formed from this iteration. For each image pixel, the values of the two images are compared and the minimum value is selected:

$$\mathrm{Im}_l = \min\left\langle I_l, \mathrm{Im}_{l-1} \right\rangle, \qquad 2 \le l \le M, \tag{23}$$

where Im_l is the intermediate resulting image at *(i)*th iteration. Note that equation 14 is defined for $2 \le l \le M$. For the first iteration (*l=1),* Im_0 is initialized with a very large values, so that the intermediate resulting image $\mathrm{Im}_1 = \min\left\langle I_1, \mathrm{Im}_0 \right\rangle = I_1$.

After step 7, the algorithm returns to step 4 to continue with the next iteration until the M^{th} iteration is finished. The intermediate resulting image is also sent to the display routine for visualizing the image. Figure 41 illustrates the compressive image and the intermediate resulting image generated in the first three iterations. Figure 42 shows the results at various iterations. In the resulting image at iteration 50, the sidelobes are significantly suppressed while the responses of the two targets remained virtually unchanged.

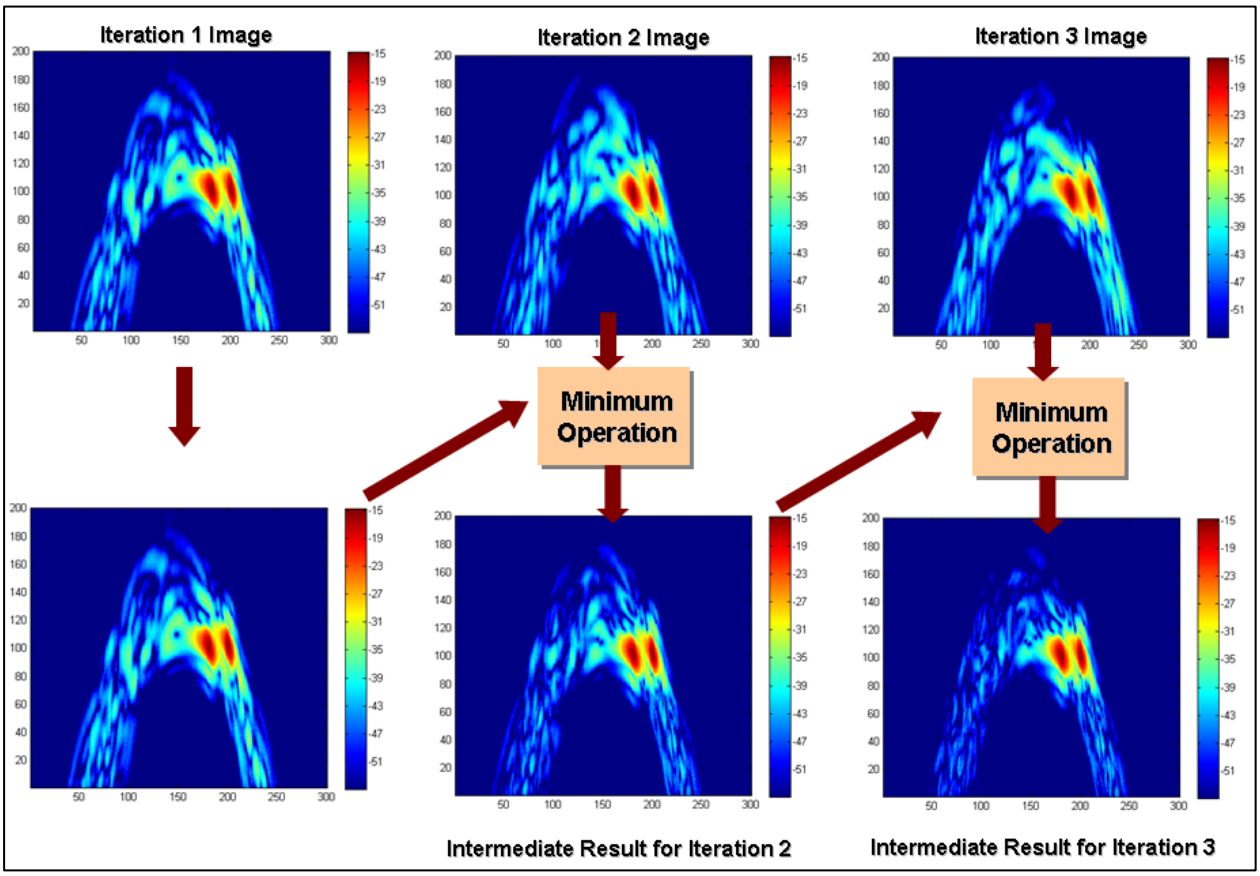

Figure 41. The compressive image and the intermediate resulting image generated in the first three iterations.

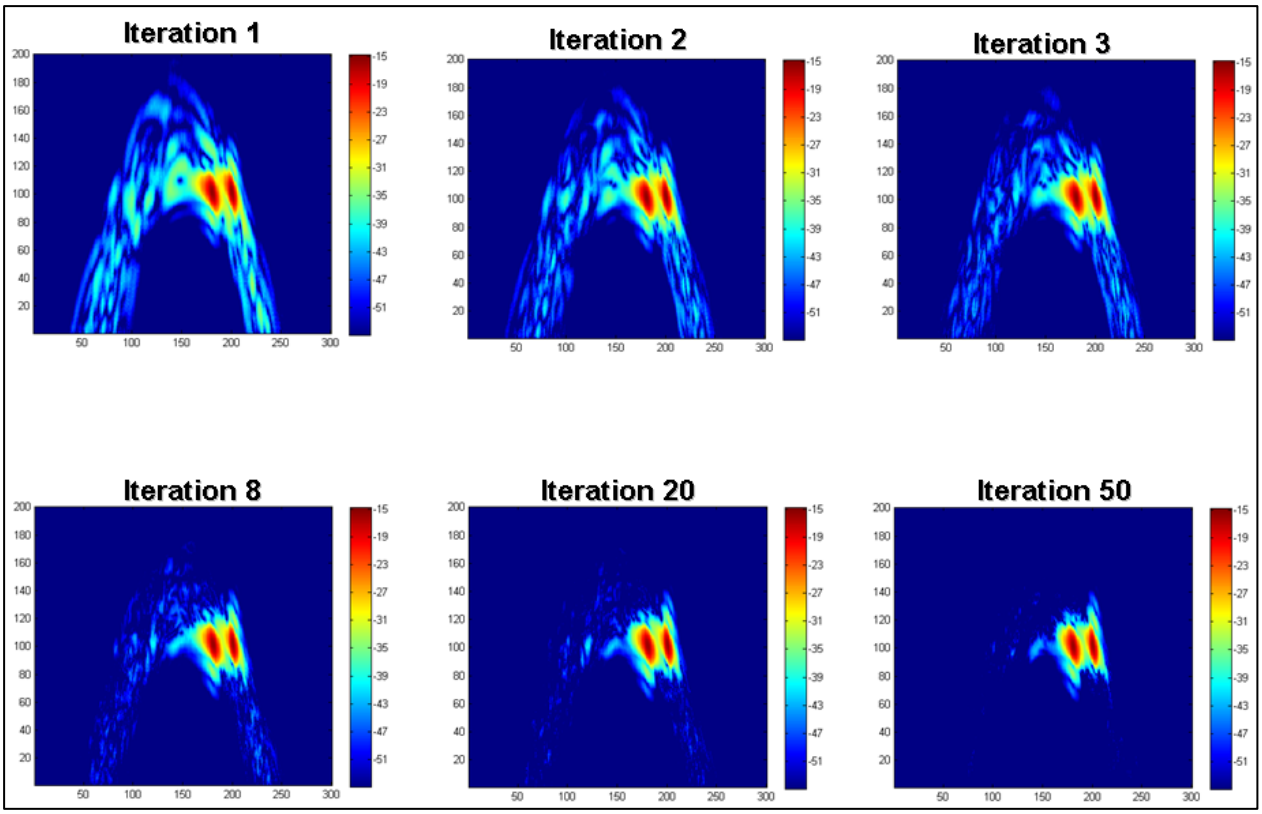

Figure 42. Results at various iterations.

Figure 43 shows the “before” and “after” images when the RSM technique is applied to the SIRE radar data in forward-looking configuration. Both SAR images are displayed using a wide dynamic range of 40 dB. We can see the background noise floor of the RSM image (figure 43, right) is significantly reduced compared to that of the baseline SAR image (figure 43, left), while the target amplitudes remain virtually unchanged. Analysis of the histograms of image pixel values from both SAR image has shown that we have achieved 12 dB—a significant improvement—in the reduction of the multiplicative noise floor.

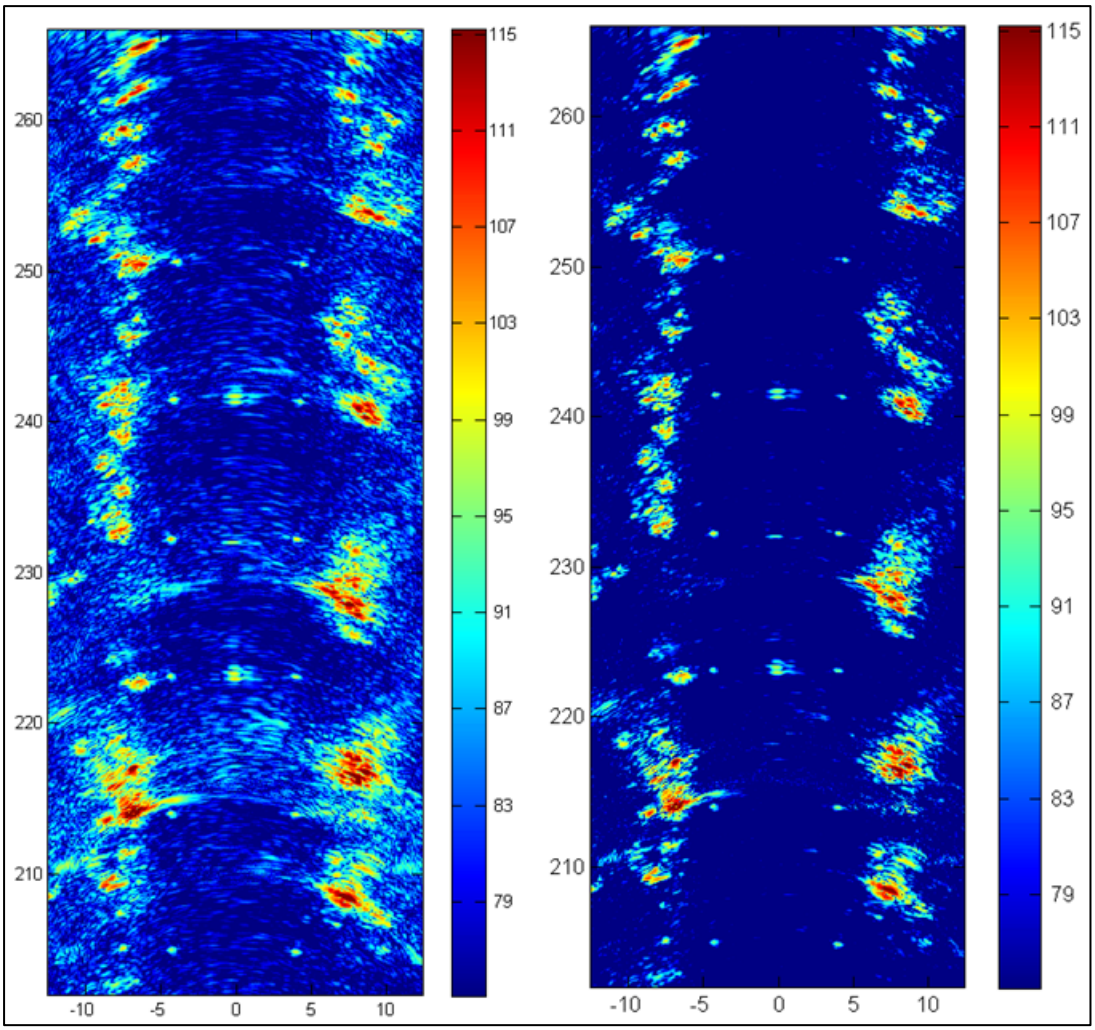

Figure 43. The “before” and “after” images when the RSM technique is applied to the SIRE radar data in forward-looking configuration. Both SAR images are displayed using a wide dynamic range of 40 dB.

Although the algorithm is originally developed for the forward-looking radar configuration, we can apply this algorithm for any imaging geometry. Figure 44 shows the “before” and “after” SAR images when the RSM technique is applied to the BoomSAR radar data in side-looking configuration. Again the noise floor in the resulting SAR image is well suppressed with the application of the RSM technique.

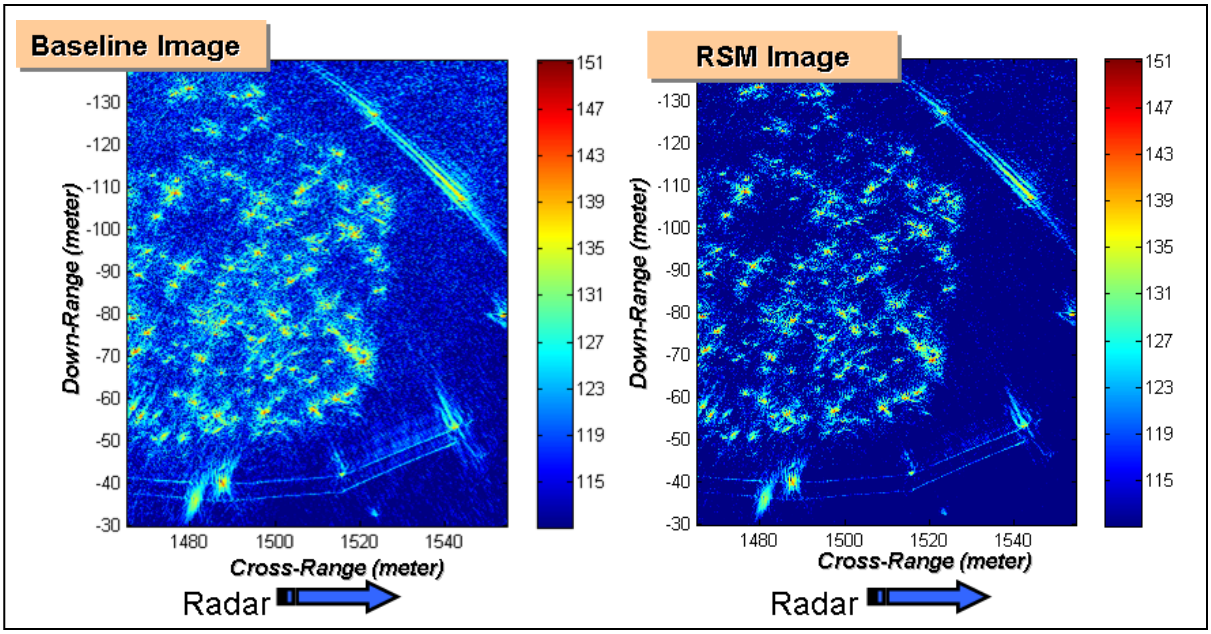

Figure 44. The “before” and “after” SAR images when the RSM technique is applied to the BoomSAR radar data in side-looking configuration.

Figure 45 summarizes the processing steps of the RSM algorithm.

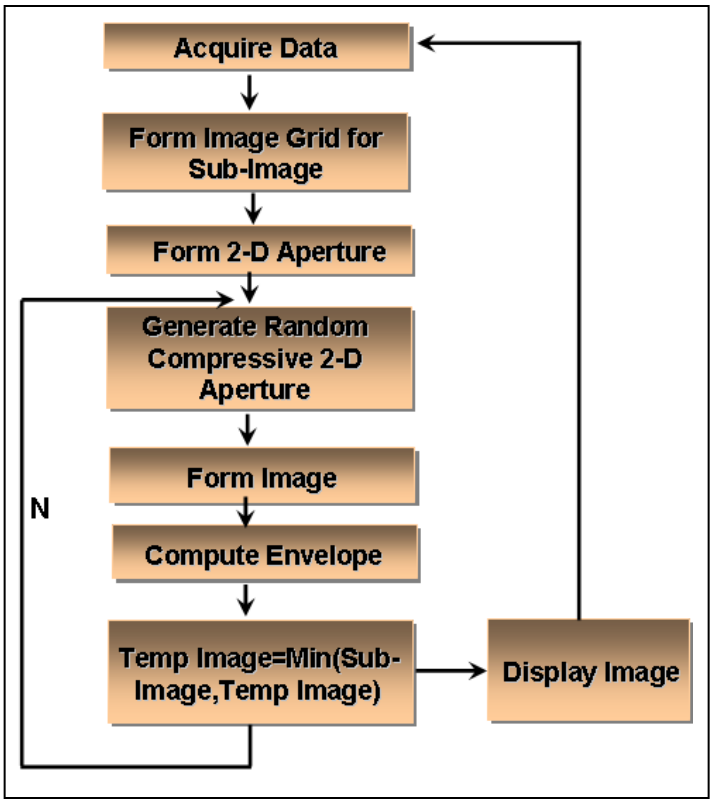

Figure 45. The processing steps of the RSM algorithm.

4. The SIRE Radar in Side-looking Mode

The SIRE radar is originally designed to support the forward-looking geometry. However, the radar can be easily converted to side-looking mode to support other missions, such as the mapping of enclosed buildings and the detection of targets and people behind walls. To convert to this side-looking mode, the antenna frame that supports two transmit antennas and 16 receive antennas is rotated 90° to be pointing in the direction that is perpendicular to the path of the vehicle (figure 46). Figure 47 shows the imaging geometry of the SIRE radar in side-looking mode. The range coverage is from 8 to 34 m. In theory, we only need one transmit element and one receive element to support the side-looking mode since the aperture is completely synthesized by the motion of the radar platform. However, the array of receive antennas give us two advantages: (1) better sampling along the aperture and (2) support for Space-Time Adaptive Processing (STAP).

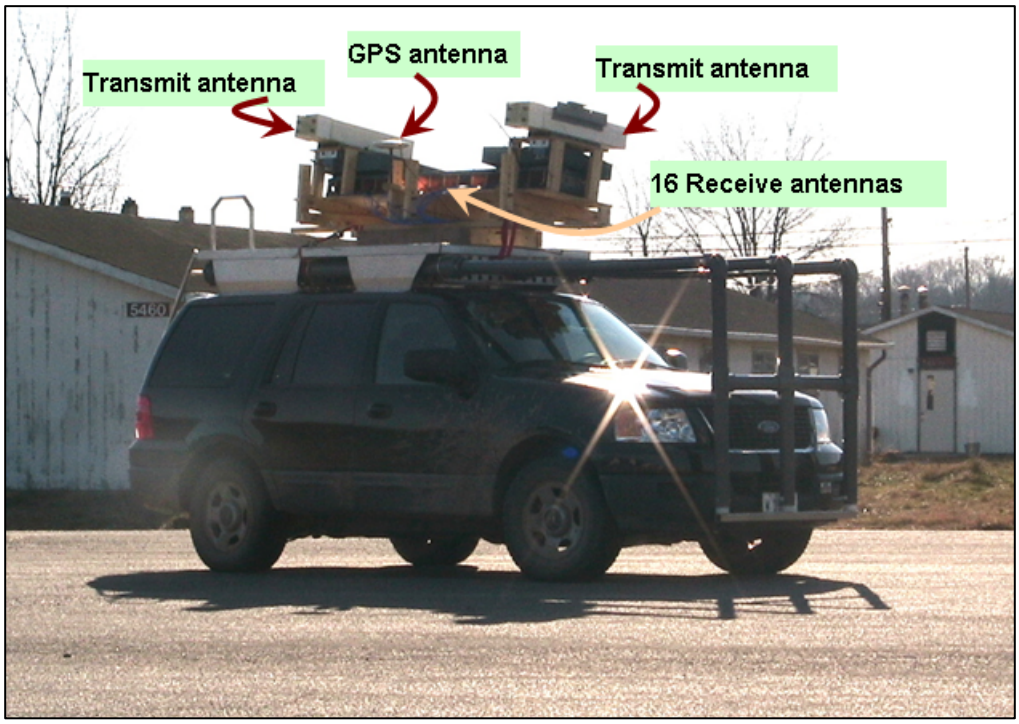

Figure 46. The SIRE radar in side-looking mode.

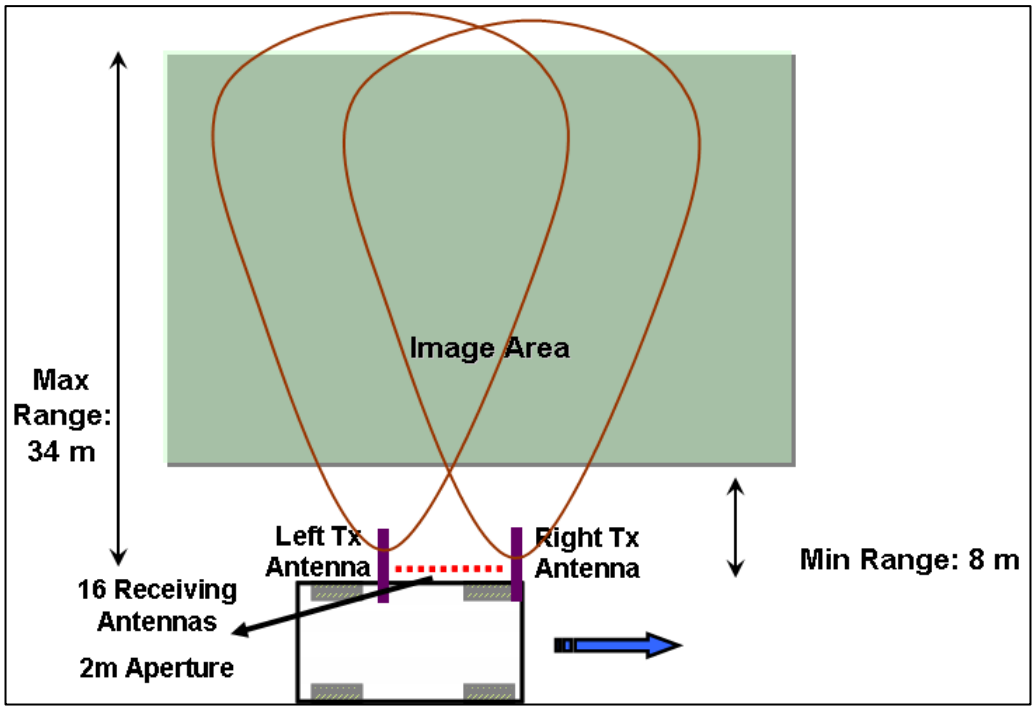

Figure 47. ARL UWB SIRE radar imaging geometry in side-looking mode.

Figure 48 shows the block diagram of the signal processing steps for the SIRE radar in side-looking mode. It is similar to figure 13 for the forward-looking mode with some modifications: (1) the Forward Motion Processing block from figure 13 is replaced with the Multipath Signal Suppression block in figure 48, and (2) the Mosaic Backprojection Image Formation block from figure 13 is replaced with the Constant Resolution Backprojection Image Formation block in figure 48. The multipath signal suppression will be described later in this section. Note that the SAR images in this report are formed using the true constant resolution backprojection algorithm (*16*), in which every pixel within the SAR image is integrated using a different sub-aperture to ensure the constant cross-range resolution across the entire image. This is especially important in this imaging geometry since the radar illuminates the building from a close distance (10 m) and generates a range swath of 30 m.

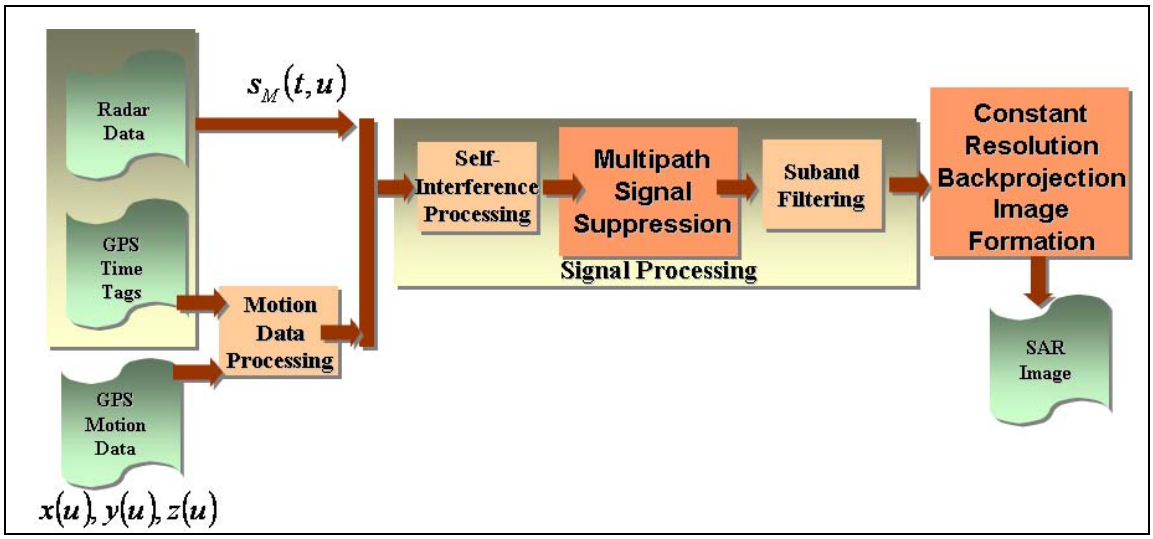

Figure 48. The block diagram of the signal processing steps for the SIRE radar in side-looking mode.

We conducted an experiment at the Aberdeen Proving Ground (APG), MD, in the housing area of the base. An abandoned barracks building was used for the experiment. The building is largely empty of furnishings, but it does have some individual rooms that provide additional structure to examine the imagery. The building can best be described as resembling the capital letter “H” with the bathrooms and showers located in the horizontal line connecting the two living quarters, which form the verticals of the “H”. There is a shingled, peaked roof over each of these legs. While many of the bathroom fixtures have been removed, the plumbing, the electrical wiring, and the heating, ventilation, and air-conditioning (HVAC) system and ductwork are still in place. A large metal fuel tank is located outside, centered between the two housing areas. An exploded view of the building can be seen in the model of figure 49. The radar illuminates the building from two directions (figure 4) by making two separate paths. For the first path it moves parallel to the long side of the barracks building and illuminates the building area along its path. At the end of the first path, the radar platform turns left and illuminates the area along the short side of the building.

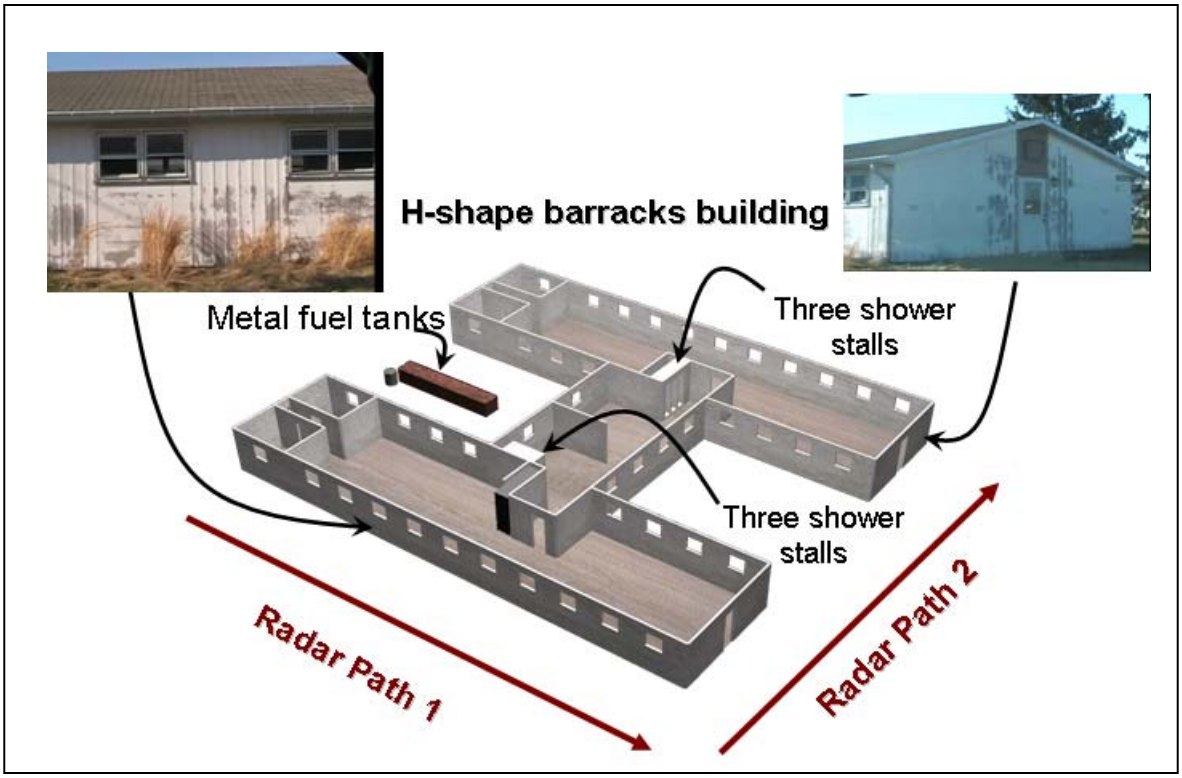

Figure 49. Sensing-through-the-wall (STTW) experiment at APG.

Figure 50 shows the initial SAR image formed using the data collected from radar path 1. This image is formed without the signal processing step to suppress the multipath signal. We noticed two artifacts from the image. First, the mismatch between the transmitter and the transmitting antenna results in the second transmitting pulse being much weaker than the original transmitting pulse. This artifact is more noticeable for large RCS objects such as the exterior wall and the metal fuel tank. Second, there is a ghost response in the image at around 20 m in downrange and is running almost parallel to the exterior wall. This response is actually formed by the backscatter from the exterior wall with respect to the second bounce from the radar platform, as illustrated in figure 51. Note that this ghost response is not exactly parallel to the exterior wall since its location is a function of both the radar location and the exterior wall location. Since the radar path does not form a perfectly parallel line with the exterior wall, this results in this multipath response that is not perfectly parallel to the exterior wall. Using the radar imaging geometry, the processing algorithm continuously tracks large responses from the radar data, estimates the range gate locations of the transmitter artifact and the second reflection, and suppresses the corresponding range gates in the prefocus radar data. This processing technique would not have substantial influence on individual targets since each target is coherently integrated over a unique aperture segment.

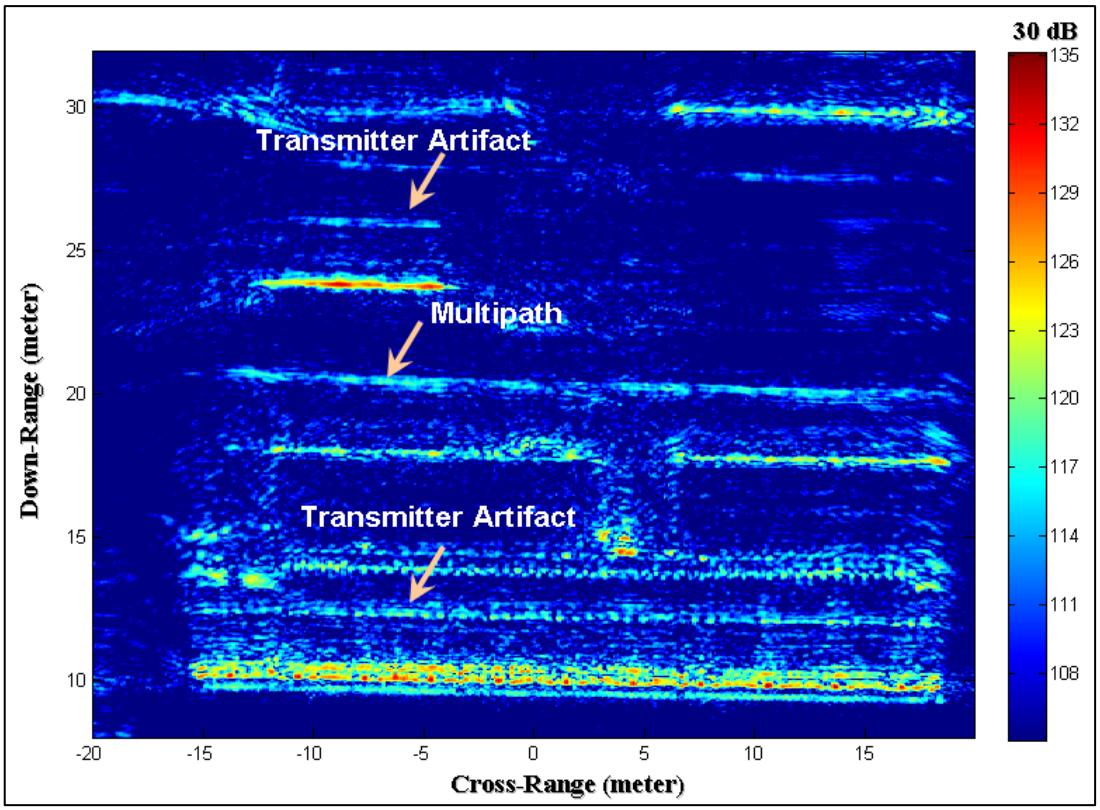

Figure 50. The initial SAR image formed using the data collected from radar path 1.

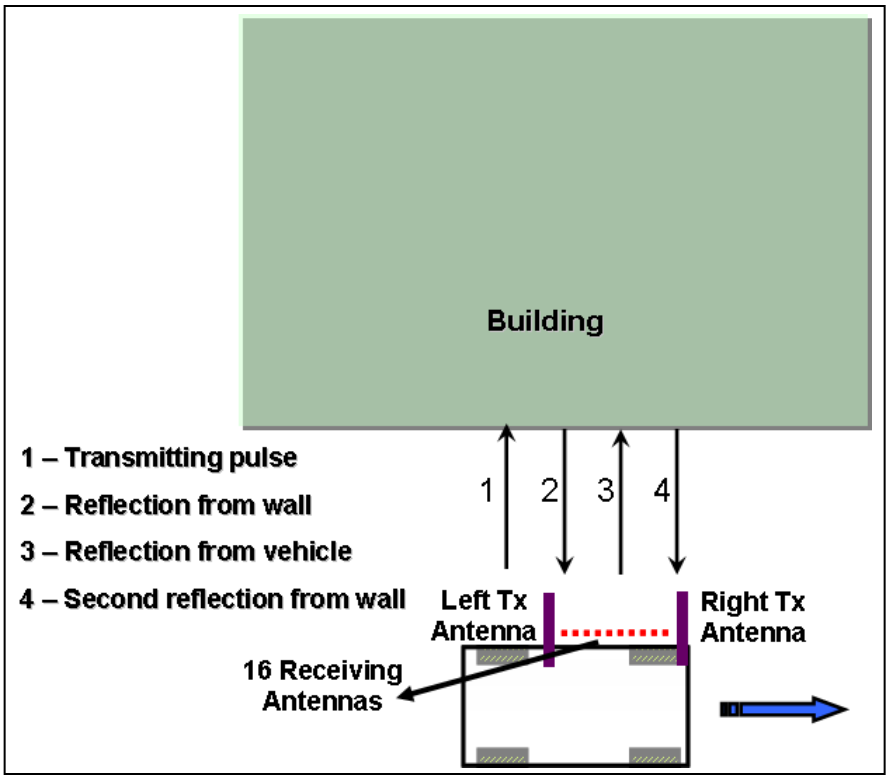

Figure 51. Illustration of multipath signal that shows up as artifact in image.

Figure 52 shows the same SAR image as in figure 50, except that the artifacts from the transmitter and the multipath signal are suppressed. Figure 53 shows the combined SAR image using data collected from both radar path 1 and path 2. This is the building mapping SAR image created by illuminating the building in two different directions. The image clearly shows the outline of the building as well as its internal structure. The back wall of the rear building and the left walls of both front and rear buildings do not show up in the image since they are out of the radar's range with respect to the two paths that the radar makes.

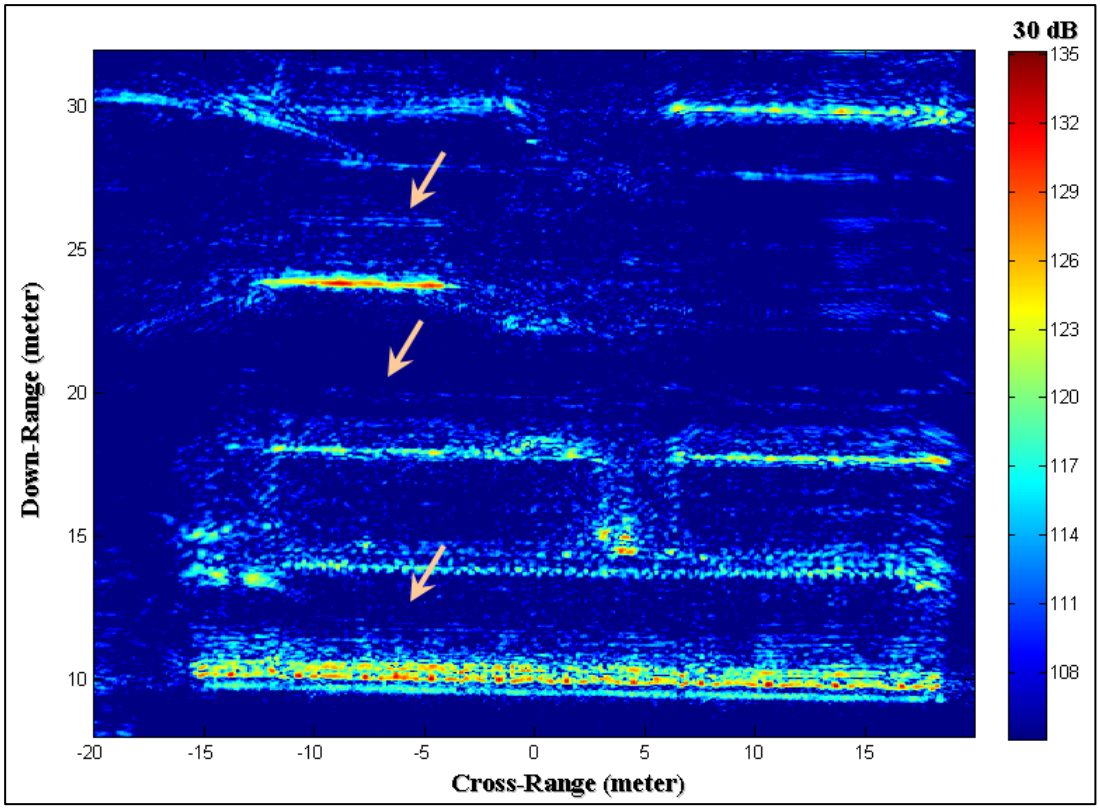

Figure 52. The same SAR image as in figure 50 except that the artifacts from the transmitter and the multipath signal are suppressed.

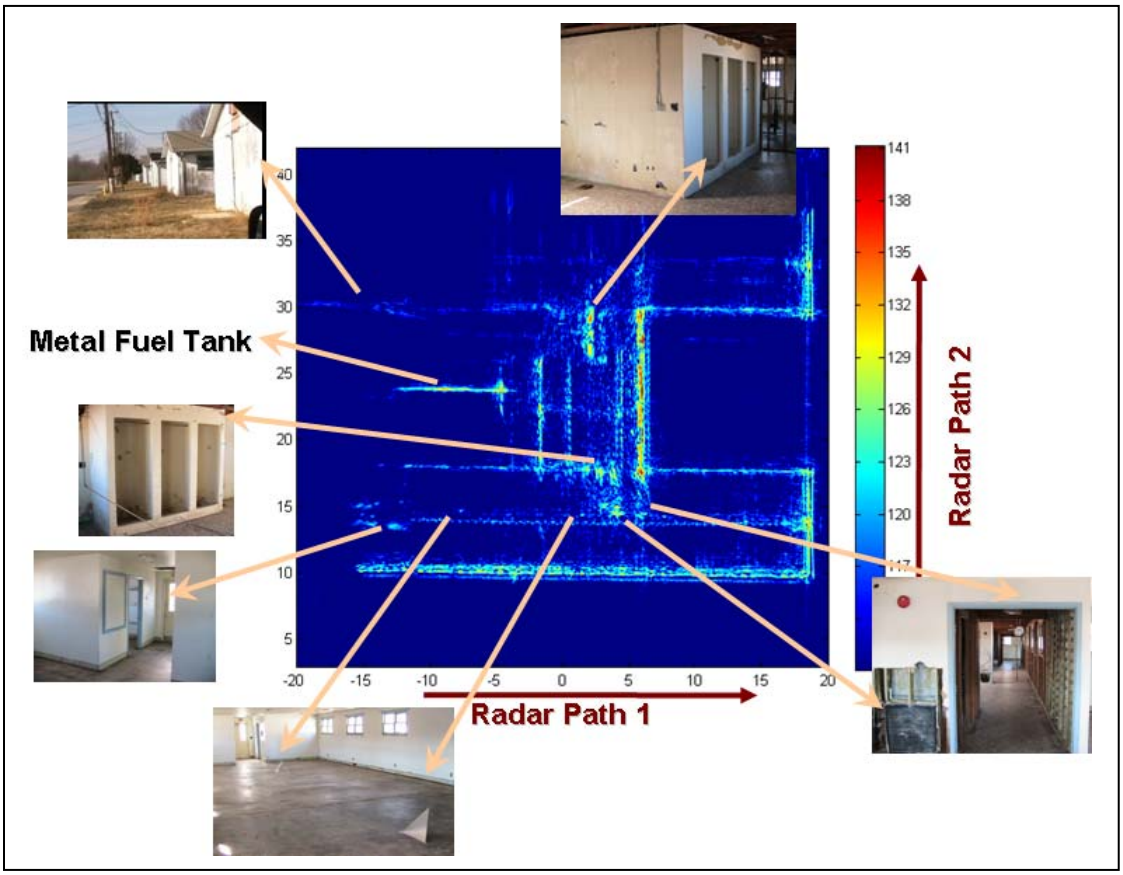

Figure 53. The combined SAR image using data collected from both radar path 1 and path 2.

5. Conclusion

UWB low-frequency radar systems are effective in detecting targets obscured by foliage and ordnance buried beneath the surface. In addition, they are also effective for mapping enclosed buildings and detecting targets and people behind walls. This unique ability to detect targets would complement other technologies to improve the survivability of vehicles using this technology and would consequently increase the overall effectiveness of the warfighter in the battlefield.

ARL has designed and constructed a new low-frequency UWB forward-imaging SAR system, and conducted several experiments in both forward-looking and side-looking modes to demonstrate the potential of this radar technology to serve these missions. In addition to the radar hardware, we also developed a suite of signal processing and image formation algorithms that provide us with high quality radar data and SAR imagery. Particularly, using a nonconventional signal processing technique, we have developed the RSM technique, which has been demonstrated to significantly suppress the multiplicative noise in the resulting SAR imagery.

This results in the ability to reliably detect small RCS targets that are often embedded in the sidelobes of large natural and manmade clutter objects. These promising results may potentially offer additional capability for vehicles for improved mobility and survivability on the battlefield.

6. References

1. Nguyen, L.; Wong, D.; Ressler, M.; Koenig, F.; Stanton, B.; Smith, G.; Sichina, J.; Kappra, K. Obstacle Avoidance and Concealed Target Detection Using the Army Research Lab Ultra-Wideband Synchronous Impulse Reconstruction (UWB SIRE) Forward Imaging Radar. *Proceedings of SPIE, Detection and Remediation Technologies for Mines and Minelike Targets XII, Vol. 6553,* April 2007.

2. Nguyen, L.; Ressler, M.; Sichina, J. Sensing Through the Wall Imaging Using the Army Research Lab Ultra-wideband Synchronous Impulse Reconstruction (UWB SIRE) Radar. *Proceedings of SPIE, Radar Sensor Technology XII, Vol. 6947,* April 2008.

3. Ressler, M.; Nguyen, L.; Koenig, F.; Wong, D.; Smith, G. The Army Research Laboratory (ARL) Synchronous Impulse Reconstruction (SIRE) Forward-Looking Radar. *Proceedings of SPIE, Unmanned Systems Technology IX, Vol. 6561,* May 2007.

4. Nguyen, L.; Soumekh, M. System Trade Analysis for an Ultra-wideband Forward Imaging Radar. *Proceedings of SPIE, Unmanned Systems Technology VIII, Vol. 6230,* 2006.

5. Real-Time Versus Equivalent-Time Sampling, Tektronix, http://www2.tek.com/cmswpt/tidetails.lotr?ct=TI&cs=apn&ci=14295&lc=EN (accessed 31 March 2009).

6. Nguyen, L. H.; Ton, T.; Wong, D.; Soumekh, M. Adaptive Coherent Suppression of Multiple Wide-bandwidth RFI Sources in SAR. *Proceedings of SPIE Int. Soc. Opt. Eng. Vol. 5427*, 1, 2004.

7. Miller, T. R.; McCorkle, J. W.; Potter, L. C. Near-least-squares Radio Frequency Interference Suppression. *Proceedings of SPIE, Vol. 2487,* 72, 1995.

8. Nguyen, L.; Soumekh, M. Suppression of Radio Frequency Interference (RFI) for Equivalent Time-sampling Ultra-wideband Radar. *Proceedings of SPIE, Algorithms for Synthetic Aperture Radar Imagery XII*, 2005.

9. Nguyen, L.; McCorkle, J.; Sichina, J. *Self-Interference Extraction Algorithm for Ultra-Wideband Synthetic Aperture Radar*; R-SRL-SE-RU-96-003; Microwave Branch, Dec 1996

10. Nguyen, L. *Signal Processing Technique to Remove Signature Distortion in ARL Synchronous Impulse Reconstruction (SIRE) Ultra-Wideband (UWB) Radar*; ARL-TR-4404; U.S. Army Research Laboratory: Adelphi, MD, March 2008.

11. McCorkle, J.; Nguyen, L. *Focusing of Dispersive Targets Using Synthetic Aperture Radar*; ARL-TR-305; U.S. Army Research Laboratory: Adelphi, MD, Aug 1994.

12. Nguyen, L. H.; Kappra, K. A.; Wong, D. C.; Kapoor, R.; Sichina, J. Mine Field Detection Algorithm Utilizing Data from an Ultrawideband Wide-area Surveillance Radar. *Proceedings of SPIE 3392*, 627, 1998.

13. Nguyen, L. H.; Kapoor, R.; Sichina, J. Detection Algorithms for Ultrawideband Foliage-penetration Radar. *Proceedings of SPIE 3066*, 165, 1997.

14. Nguyen, L. H.; Ton, T. T.; Wong, D. C.; Ressler, M. A. Signal Processing Techniques for Forward Imaging Using Ultrawideband Synthetic Aperture Radar. *Proceedings of SPIE 5083*, 505, 2003.

15. Nguyen, L.; Sichina, J. Method and System for Forming an Image with enhanced contracts and/or reduced noise. U.S. Patent 12/331888, Dec 2008.

16. Nguyen, L.; Sichina, J. SAR Image Formation Using Phase-History Data from Non-Uniform Aperture. *Proceedings of SPIE, Radar Sensor Technology XI, Vol. 6547*, May 2007.

List of Symbols, Abbreviations, and Acronyms

2-D	two-dimensional
3-D	three-dimensional
A/D	analog-to-digital
ADC	analog-to-digital converter
APG	Aberdeen Proving Ground
ARL	U.S. Army Research Laboratory
COTS	commercial-off-the-shell
GPS	global positioning system
HVAC	heating, ventilation, and air-conditioning
PC	personal computer
PRF	pulse repetition frequency
PRI	pulse repetition interval
RCS	radar cross section
RF	radio frequency
RFI	RF interference
RSM	Recursive Sidelobe Minimization
SAR	synthetic aperture radar
SIRE	synchronous impulse reconstruction
TEM	transverse electromagnetic
UWB	ultra-wideband
VME	Versa Module Europa

No. of Copies	Organization
1 PDF	DEFENSE TECH INFO CTR ATTN DTIC OCA 8725 JOHN J KINGMAN RD STE 0944 FT BELVOIR VA 22060-6218
1	DARPA ATTN IXO S WELBY 3701 N FAIRFAX DR ARLINGTON VA 22203-1714
1 CD	OFC OF THE SECY OF DEFNS ATTN ODDRE (R&AT) THE PENTAGON WASHINGTON DC 20301-3080
1	US ARMY RSRCH DEV AND ENGRG CMND ARMAMENT RSRCH DEV AND ENGRG CTR ARMAMENT ENGRG AND TECHNLGY CTR ATTN AMSRD AAR AEF T J MATTS BLDG 305 ABERDEEN PROVING GROUND MD 21005-5001
1	PM TIMS, PROFILER (MMS-P) AN/TMQ-52 ATTN B GRIFFIES BUILDING 563 FT MONMOUTH NJ 07703
1	US ARMY INFO SYS ENGRG CMND ATTN AMSEL IE TD F JENIA FT HUACHUCA AZ 85613-5300
1	COMMANDER US ARMY RDECOM ATTN AMSRD AMR W C MCCORKLE 5400 FOWLER RD REDSTONE ARSENAL AL 35898-5000
1	US GOVERNMENT PRINT OFF DEPOSITORY RECEIVING SECTION ATTN MAIL STOP IDAD J TATE 732 NORTH CAPITOL ST NW WASHINGTON DC 20402
4	US ARMY RSRCH LAB ATTN AMSRD ARL CI HC B HENZ ATTN AMSRD ARL CI HC D SHIRES ATTN AMSRD ARL CI HC S PARK ATTN AMSRD ARL CI HC J ROSS ABERDEEN PROVING GROUND MD 21005
1	US ARMY RSRCH LAB ATTN AMSRD ARL CI OK TP TECHL LIB T LANDFRIED BLDG 4600 ABERDEEN PROVING GROUND MD 21005-5066
1	DIRECTOR US ARMY RSRCH LAB ATTN AMSRD ARL RO EV W D BACH PO BOX 12211 RESEARCH TRIANGLE PARK NC 27709
17	US ARMY RSRCH LAB ATTN AMSRD ARL CI OK PE TECHL PUB ATTN AMSRD ARL CI OK TL TECHL LIB ATTN AMSRD ARL SE RU A SULLIVAN ATTN AMSRD ARL SE RU K KAPPRA ATTN AMSRD ARL SE RU L NGUYEN (10 copies) ATTN AMSRD ARL SE RU M RESSLER ATTN AMSRD ARL SE RU J COSTANZA ATTN IMNE ALC HRR MAIL & RECORDS MGMT ADELPHI MD 20783-1197
Total	31 (29 HC, 1 CD, 1 PDF)